X-raying the Ultraluminous Infrared Starburst Galaxy and Broad Absorption Line QSO, Markarian 231, with *Chandra.*

S. C. Gallagher, W. N. Brandt, G. Chartas, G. P. Garmire,

Department of Astronomy and Astrophysics
The Pennsylvania State University
University Park, PA 16802
gallsc, niel, chartas, garmire@astro.psu.edu

and

R. M. Sambruna

Department of Physics & Astronomy and School of Computational Sciences
George Mason University
4400 University Drive M/S 3F3
Fairfax, VA 22030-4444
rms@physics.gmu.edu

ABSTRACT

With 40 ks of *Chandra* ACIS-S3 exposure, new information on both the starburst and QSO components of the X-ray emission of Markarian 231, an ultraluminous infrared galaxy and Broad Absorption Line QSO, has been obtained. The bulk of the X-ray luminosity is emitted from an unresolved nuclear point source, and the spectrum is remarkably hard with the majority of the flux emitted above 2 keV. Most notably, significant nuclear variability (a decrease of $\sim 45\%$ in approximately 6 hours) at energies above 2 keV indicates that *Chandra* has probed within light hours of the central black hole. Though we concur with Maloney & Reynolds that the direct continuum is not observed, this variability coupled with the 188 eV upper limit on the equivalent width of the Fe Kα emission line argues against the reflection-dominated model put forth by these authors based on their *ASCA* data. Instead, we favor a model in which a small, Compton-thick absorber blocks the direct X-rays, and only indirect, scattered X-rays from multiple lines of sight can reach the observer. Extended soft, thermal emission encompasses the optical extent of the galaxy and exhibits resolved structure. An off-nuclear X-ray source with a 0.35–8.0 keV luminosity of $L_X = 7 \times 10^{39}$ erg s^{-1}, consistent with the ultraluminous X-ray sources in other nearby starbursts, is detected. We also present an unpublished FOS spectrum from the *HST* archive showing the broad C IV absorption.

Subject headings: galaxies: active — galaxies: individual (Mrk 231, UGC 08058) — galaxies: starburst — X-rays: galaxies

1. Introduction

The extraordinary galaxy Markarian 231 was discovered in 1969 as part of a survey searching for galaxies with strong ultraviolet continua (Markarian 1969). With the first spectrum, it was identified as unique among the Markarian sample be-cause of deep, blue-shifted Na D absorption evocative of broad absorption line quasi-stellar objects (BAL QSOs; Arakelian et al. 1971). Soon after, Adams & Weedman (1972) also identified broad absorption lines from Ca II H and K and He I at the same velocity as the Na D system. In addi-

tion, they first described the long tidal tails and disturbed morphology of the galaxy.

Since those early observations, Mrk 231 has maintained its reputation as an exceptional object and continues to be a favorite target in all wavelength regimes. Years before the *Infrared Astronomical Satellite* (*IRAS*) was launched, Mrk 231 was known to have an infrared luminosity on a par with QSOs ($\sim 4 \times 10^{12}$ $L_\odot$; Rieke & Low 1972, 1975). Weedman (1973) initially proposed that this energy could be non-thermal ultraviolet emission reradiated thermally by dust. Even after *IRAS* expanded the known population of ultraluminous infrared galaxies, Mrk 231 remains one of the most luminous and the most powerful known at $z < 0.1$ (e.g., Surace et al. 1998).

An association of Mrk 231 with BAL QSOs was suggested from the start (Arakelian et al. 1971), but confirmation of this status required ultraviolet spectroscopy. The first published *International Ultraviolet Explorer* (*IUE*) spectra showed no obvious C IV or Mg II emission or absorption, but the signal-to-noise ratio of the data was low (Hutchings & Neff 1987). *Hubble Space Telescope* (*HST*) ultraviolet spectra confirmed the BAL QSO identification of Mrk 231 with the discovery of broad Mg II and Fe II absorption (Smith et al. 1995). Broad absorption lines are found in $\sim 10\%$ of optically selected QSOs, but Mg II BAL QSOs only comprise $\sim 10\%$ of that population. Other spectral characteristics that Mrk 231 shares with low-ionization BAL QSOs include reddened optical and ultraviolet continua (e.g., Boksenberg et al. 1977; Hutchings & Neff 1987), strong optical Fe II emission (e.g., Adams & Weedman 1972; Boksenberg et al. 1977), and weak [O III] emission (e.g., Boroson & Meyers 1992).

Though the emission of many ultraluminous infrared galaxies appears to be dominated by energetic starbursts, Mrk 231 has been repeatedly identified as an exception (e.g., Goldader et al. 1995; Krabbe et al. 1997; Rigopoulou et al. 1999), and many pieces of evidence point toward an accreting black hole as the major power source behind the enormous infrared luminosity (though see Downes & Solomon 1998 for an alternate view). The optical spectrum exhibits broad Hα (FWHM = 2870 km s^{-1}; e.g., Boroson & Meyers 1992) and asymmetric Hβ emission. The bright nuclear source is unresolved at radio, infrared,

and optical wavelengths (e.g., Ulvestad, Wrobel, & Carilli 1999; Lai et al. 1998; Surace & Sanders 1999), and a parsec-scale radio jet with low apparent speeds has been resolved with Very Long Baseline Array (VLBA) observations (Ulvestad et al. 1999). Variability on time scales of years has been observed in the radio emission (Ulvestad et al. 1999) and in the Na D and He I absorption lines (Boroson et al. 1991; Kollatschny et al. 1992; Forster et al. 1995). The *IRAS* color, F_{25}/F_{60} (the ratio of the flux density at 25 μm to that at 60 μm), is characterized as "warm" (> 0.25), $F_{25}/F_{60} = 0.29$ (e.g., Low et al. 1988). This implies a non-thermal continuum or warm dust, more likely to result from the hard ionizing continuum of an active nucleus. In addition, the ratio of infrared luminosity to mass in H$_2$, $L_{\rm IR}/M_{\rm H_2} = 225$ $L_\odot$ $M_\odot^{-1}$, is difficult to explain without a powerful QSO contributing the bulk of the infrared luminosity (Sanders, Scoville, & Soifer 1991).[1] In *HST* images, the point-like nucleus has colors inconsistent with a starburst, and $M_B \sim -21.6$ with no correction for reddening (Surace et al. 1998). From the shape of the optical and ultraviolet continua and infrared line ratios, the reddening is estimated to be $A_V \sim 2$ mag (Boksenberg et al. 1977; Cutri et al. 1984). Correcting for reddening then places Mrk 231 at QSO luminosities ($M_B \lesssim -24$) that can account for the infrared energy (e.g., Surace et al. 1998).

Though the primary power behind the incredible far-infrared luminosity of Mrk 231 is almost certainly an active nucleus, the galaxy is also undergoing an energetic starburst. The $B - R$ colors of optical knots are indicative of active, early-type star formation (Hutchings & Neff 1987), and *HST* images of the nucleus clearly resolved blue, star-forming knots (Surace et al. 1998). Most dramatically, in the inner kiloparsec, a nuclear ring of active star formation with a rate estimated to be > 100 $M_\odot$ yr^{-1} has been studied with Very Large Array and VLBA observations (Carilli et al. 1998; Taylor et al. 1999). Furthermore, Sanders et al. (1987) observed CO emission suggestive of many spiral galaxies worth of concentrated molecular gas that has since been mapped with high

---

[1] For reference, the total Sanders et al. (1991) sample has a median value of $L_{\rm IR}/M_{\rm H_2} \approx 26$ $L_\odot$ $M_\odot^{-1}$, and NGC 4418, the galaxy with the next highest value after Mrk 231, has $L_{\rm IR}/M_{\rm H_2} = 89$ $L_\odot$ $M_\odot^{-1}$.

resolution by Bryant & Scoville (1996). The optical morphology of Mrk 231 is irregular, and the asymmetries in the structure of the host galaxy are likely the result of a merger. Tidal tails extending more than $30''$ to the North and South of the galaxy clearly visible in deep images further support the merger scenario. The combination of starburst and luminous QSO make Mrk 231 a classic example of the transition from starburst to QSO in the paradigm outlined by Sanders et al. (1988).

X-ray studies of ultraluminous infrared galaxies are essential since they provide a direct probe not only of the environment of an active nucleus but also of the end-products of stellar evolution. Mrk 231 is of additional interest as a BAL QSO. BAL QSOs are notoriously weak X-ray sources, and few X-ray spectra of them exist in the literature. Since the *HEAO-1* and *Einstein* era, Mrk 231 has been identified as anomalously X-ray weak given the implied power of its active nucleus (Eales & Arnaud 1988; Rieke 1988). Mrk 231 was first detected in X-rays with the *ROSAT* Position Sensitive Proportional Counter (PSPC; Rigopoulou et al. 1996), and extended emission was observed with the High Resolution Imager (HRI; Turner 1999). *ASCA* observed this source twice, and spectral analysis indicated both starburst and non-thermal emission in the X-rays (Iwasawa 1999; Turner 1999). With the most recent 100 ks *ASCA* observation, Maloney & Reynolds (2000) argued that the hard X-ray spectrum is dominated by X-rays "reflected" from neutral or nearly neutral material, and they modeled an Fe Kα emission line with EW$\approx$ 290 eV. In this model, the obscuration to the nucleus is so severe that no direct X-rays below ~ 10 keV escape along the line of sight. This implies an absorption column density $\gtrsim 10^{24}$ cm^{-2} and suggests an intrinsic X-ray luminosity more typical of a luminous QSO, although the precise value is highly uncertain.

In this paper, we present a *Chandra* ACIS-S3 observation of Mrk 231. Previous X-ray spectral analysis of this target has been confused by the overlap of the starburst and nuclear components due to the large point spread functions (PSFs) of earlier X-ray missions. With the excellent $1''$ spatial resolution of *Chandra*, the nuclear and disk components can be spatially separated for spectral analysis. At $z = 0.042$, $1''$ is approximately 0.8 kpc for $H_0 = 75$ km s^{-1} Mpc^{-1} and $q_0 = \frac{1}{2}$. The low Galactic column density, $N_{\mathrm{H}} = (1.03 \pm 0.10) \times 10^{20}$ cm^{-2} (Elvis, Lockman, & Wilkes 1989), also makes Mrk 231 an excellent target for studying the soft X-rays of an active starburst galaxy.

2. Observations and Data Reduction

Mrk 231 was observed with the back-illuminated *Chandra* ACIS-S3 detector (G. P. Garmire et al., in preparation) for 39.8 ks on 2000 October 19. The data were processed with the standard *Chandra* X-ray Center (CXC) pipeline from which the level 1 events file was used. The data were filtered on good time intervals resulting in a "live" exposure of 39.3 ks. The standard pipeline processing introduces a $0''.5$ software randomization into the event positions, which degrades the spatial resolution by $\approx 12\%$ (Chartas et al. 2002). This randomization is done to avoid aliasing effects noticeable in observations with exposure times less than ~ 2 ks. As spatial resolution was crucial for our analysis and our observation was significantly longer, we removed this randomization by recalculating the event positions in sky coordinates using the CIAO 2.0 tool, acis_process_events. The data were filtered to keep "good" *ASCA* grades (grades 0, 2, 3, 4, and 6). Filtering on "status" removed ~ 30 X-ray events from the nucleus because X-rays were inappropriately tagged as cosmic ray afterglows. Therefore, the values in the status column for cosmic ray afterglows were ignored for the final filter on "good" status.

In order to evaluate the reliability of our subsequent analysis, we checked the data for evidence of pile-up. Pile-up occurs when two or more photons arrive at a pixel during a single, 3.2 s frame and alters the spectrum and PSF. In the raw and processed data, there was no indication of a read-out streak (due to X-rays from a bright source which arrived as the CCD was being read out), which would indicate a count rate sufficient to result in significantly piled-up data. However, given the observed count rate of the nucleus (0.039 ct s^{-1}), this source is within the regime where pile-up at the $\sim 5\%$ level is a possibility. At this low level, our statistical errors are likely to be greater than any effects of pile-up. Throughout this paper, wherever the analysis could be sensitive to the ef-

fects of pile-up, we carefully test our results. The complete analysis of the possible effects of pile-up, which requires detailed spectral information, is deferred to §5.1.6.

The light curve of the entire CCD was examined for evidence of variability. The background did flare by a factor of 2–3 for ~ 2.2 ks near the end of the observation. For spectral analysis of diffuse emission and image analysis, this time interval was removed leaving a total of ~ 800 counts in this region. The count rate of the nuclear source in Mrk 231 was high enough, and the source cell region small enough, that the increase in background was not significant, and so the higher background times were kept for the nuclear light curve and spectral analysis. The nuclear source cell contained a total of ~ 1450 counts; over the course of the flare, less than 2 additional background counts over the entire ACIS-S3 band would be expected in a circular region with a radius of $2''$.

3. Image Analysis

3.1. Nucleus and Extended Emission

Mrk 231 is one of the 212 extragalactic sources that define the International Celestial Reference Frame, and thus coordinates accurate to $\lesssim 1$ mas are available from Very Large Baseline Interferometry (Ma et al. 1998). The centroid of the nuclear X-ray emission from Mrk 231 is within $1''$ of this position; this is within the typical absolute astrometric errors of *Chandra*.

In order to examine qualitatively the spatial structure of the X-ray emission, the events were filtered into three broad energy bands: full (0.35–8.0 keV), soft (0.35–2.0 keV), and hard (2.0–8.0 keV). The lower bound of 0.35 keV was chosen to avoid a strong feature in the instrumental background, and above ~ 8 keV the effective area of the High-Resolution Mirror Assembly (HRMA) drops while the particle background rises sharply. Examining the spatial distribution in these bands gives some indication of the emission mechanisms in different physical regions. Generally, thermal, starburst emission is soft with $kT \lesssim 2$ keV while non-thermal, nuclear emission has a harder component with emission up to and beyond the highest energies of the ACIS-S3 bandpass.

To bring out subtle features, the X-ray images were each adaptively smoothed at the 2.5σ level using the algorithm of Ebeling, White, & Rangarajan (2001). The detection of soft, extended emission with the *ROSAT* HRI (Turner 1999) is confirmed, but the superior resolution of *Chandra* enables additional structure within the galaxy to be discerned. Generally, the extended emission is asymmetric, and the nuclear source is point-like and off-center with respect to the extended emission (see Figure 1). The galaxy X-ray emission is on the same scale as the optical emission though the tidal tails are not apparent in X-rays. From a comparison of the soft and hard images (Figures 1b and 1c), the galaxy emission can be seen to be primarily soft ($E < 2.0$ keV), consistent with thermal, starburst emission. In the hard band where non-thermal emission would be expected to dominate, the emission is much more compact, and the nucleus becomes even more apparent. At all energies, the nucleus contributes significantly to the X-ray flux; this is most clearly seen in the surface plots of the adaptively smoothed soft-band and hard-band images (Figure 2).

Radial surface-brightness profiles were also calculated in order to examine quantitatively the intensity distribution; the X-ray centroid of the nuclear emission was used as the origin. Out to radii of $\sim 30''$, the galaxy emission in the soft band is above the background. However, outside of $\sim 18''$, the hard-band emission is consistent with the background level (see Figure 3a). All of the extended hard-band emission can be attributed to the wings of the PSF of the central source (see §5.1.6 for the complete analysis).

The spatial structure of the X-ray emission is not obviously correlated with optical or radio structures. In particular, the bright knots of starburst emission are not apparent in the X-rays (Figure 4). However, the X-ray emission enhancement to the Northeast (see the X-ray contours in Figure 4) of the nucleus is coincident with the contours of the $G - B$ (green) color from Hutchings & Neff (1987). These authors speculated that the green emission is likely from nebular [O III]; the structure is reminiscent of ionization cones seen in Seyfert 2 galaxies. To compare different X-ray emission mechanisms with the multi-wavelength data, we used the adaptive binning code, AdaptiveBin (Sanders & Fabian 2001), to create a hardness-ratio map. Such a map indicates the value of the hardness ratio, which is defined as

the ratio of 2.0–8.0 keV to 0.35–2.0 keV counts, at any given location. The algorithm of Sanders & Fabian (2001) calculates the hardness ratio in each pixel, and then it combines adjacent pixels until the errors (propagated from Poisson statistics) on the ratio have dropped below a given fractional tolerance. Given our small numbers of counts, we chose a moderate tolerance of 0.40; i.e., the hardness-ratio error is less than 40% in each combination of pixels. The background-subtracted, hardness-ratio map overlaid with full-band X-ray contours is displayed in Figure 5. The nuclear region spans a noticeably higher range of hardness ratios, $HR_{nuc} \approx 0.6$–1.8, than the extended galaxy ($HR_{gal} \approx 0.1$–0.4) and shows obvious small-scale structure. With the larger number of counts in this region, finer structure can be distinguished as the pixels are smaller. An inner region directly to the West of the nucleus also shows hard X-ray emission ($HR = 1.25 \pm 0.4$) which corresponds to the reddest $B - R$ contours from Hutchings & Neff (1987). This relationship suggests that the hardness is likely the result of intrinsic absorption that would also redden the optical color.

3.2. Non-Nuclear Point Sources

The CIAO 2.0 tool, wavdetect, which implements a wavelet source-detection algorithm, was used to search the full, soft, and hard-band images. Several point sources within $3'$ of the X-ray centroid of Mrk 231 were detected, but none (other than the nucleus) was found within the optical extent of the galaxy. However, visual inspection of the data suggested the presence of a point source within $3''$ of the nucleus (see Figure 6). Based on our experience with the algorithm, wavdetect is not very sensitive to faint point sources on surface-brightness gradients such as those found near bright point sources. Therefore, the lack of a wavdetect detection of this putative point source is not unreasonable.

Within a $1''$-radius source cell of the possible point source, 23 full-band counts were registered where ~ 10 are expected from the local background. This background was calculated as the mean number of counts per pixel in an annulus with an inner radius of $1''$ and an outer radius of $2''$ normalized to the area of the source cell. There is only a 0.03% chance of this occurrence due to Poisson fluctuations. For maximum sen-

sitivity, the entire observation was used for this measurement; with such a small source cell the effect of the background flare should be negligible. The errors in the source and background measurements were determined using the Poisson values for 90% confidence tabulated in Gehrels (1986); they were then added in quadrature to calculate the error in the background-subtracted source counts: $13^{+6.6}_{-4.9}$ counts for a full-band count rate of $(3.3^{+1.7}_{-1.3}) \times 10^{-4}$ ct s^{-1}. Assuming this source has a power-law slope typical of an X-ray binary, $\Gamma = 1.7$, the 0.35–8.0 keV flux, F_X, equals $(2.2^{+1.1}_{-0.8}) \times 10^{-15}$ erg cm^{-2} s^{-1}, though this value is not sensitive to the assumed model. At the redshift of Mrk 231, this corresponds to a luminosity, $L_X = (7.3^{+3.4}_{-2.8}) \times 10^{39}$ erg s^{-1}.

If this is a single point source radiating isotropically, then the Eddington limit at this luminosity suggests a massive compact object, $M = 35$–$90 \ M_\odot$. Such a source is consistent with observations of other starburst galaxies where several point sources with comparable luminosities and implied masses have been detected (e.g., Makishima et al. 2000). Alternatively, an off-nuclear point source with this flux could be a luminous supernova remnant (e.g., Schlegel 1995) such as was found in the Circinus Galaxy (Bauer et al. 2001). Given the low numbers of counts, this could also be a spatially extended area of enhanced X-ray emission such as a superbubble.

4. Variability Analysis

Nuclear light curves were examined for variability, and the full-band count rate did apparently show a subtle decrease over the course of the observation. To examine this possible variability quantitatively, the full-band event arrival times from a $2''$-radius source cell were compared with a constant count rate using the non-parametric Kolmogorov-Smirnov (K-S) test. The K-S statistic of 0.036 gave a probability of 0.042 for the data being consistent with a constant count rate. In order to investigate possible variability further, the data were divided into soft and hard bands and tested separately with the K-S test. This strategy was motivated by the different emission mechanisms contributing in different bands; the soft-band emission may have a significant starburst component while the hard-band emission should

be attributed to the active nucleus. The soft-band light curve was consistent with constant flux, and a K-S statistic of 0.033 indicated a probability of 0.353 that the data were consistent with the null hypothesis. In contrast, the hard-band light curve yielded a K-S statistic of 0.069 giving a probability of only 0.002 that the data were consistent with a constant count rate; this result is highly significant. The binned light curves are presented in Figure 7, and the bin size was chosen to obtain at least 50 counts in each bin. The hard-band bin with the lowest flux contains $55\pm10\%$ of the counts in the bin with the highest flux corresponding to a flux decrease of $45 \pm 14\%$ over 20 ks.

To investigate further the energy dependence of the variability, we applied a K-S test to the photon arrival times in different energy bands, starting with 0.35–8.0 keV. At each step, the lower limit to the energy band was increased, and the K-S test reapplied. The results of this analysis are presented in Figure 8; the energy band showing the most highly significant variability (with a K-S probability of 4.2×10^{-4}) was 2.75–8.0 keV. This energy-dependent variability can be understood either as energy bands with softer lower limits suffering from dilution by a soft, constant flux component, or as a lack of soft flux from the changing component. For example, the starburst emission, which contributes primarily to the 0.5–2.0 keV emission even within the nuclear source cell (see §5 for further discussion), is generated on physical scales of parsecs to kiloparsecs. Because of the larger scale of this emission, the flux from the starburst would not be expected to vary on time scales as short as the exposure time of this observation. In contrast, the small-scale, accretion-generated X-rays dominate the power of the nuclear emission at energies $\gtrsim 2.0$ keV. Variability on the time scale of this observation is thus much more likely to arise from this physically compact region. In the hardest bands, the number of counts decreases rapidly as a result of the smaller effective area of the telescope, thus reducing the sensitivity of the K-S test to variability.

In order to confirm that low-level pile-up was not causing false variability, the K-S test was also applied to an annular region with an inner radius of $0\rlap{.}''5$ and outer radius of $3''$. Since possible pile-up at the $\sim 5\%$ level will only affect the innermost pixels of a point source, an annular source region

is much less susceptible to pile-up, though it also contains less than half the counts in each band. As with the circular source-cell region, the hard band showed significant variability with a K-S probability of 0.013 of a constant count rate. The soft-band light curve was consistent with a constant count rate with a K-S probability of 0.892.

5. Spectral Analysis

The $1''$ spatial resolution of *Chandra* allowed us to perform spectroscopy on physically distinct regions. Throughout the spectral analysis, Galactic absorption was fixed at 1.03×10^{20} cm^{-2} (see §1). All errors are for 90% confidence with all fitted parameters taken to be of interest other than absolute normalization, unless otherwise noted. The counts, fluxes, and luminosities of different regions within the galaxy are listed in Table 1, and the spectral fitting results described within this section are summarized in Table 2.

5.1. Nucleus

5.1.1. Spectrum Extraction

Analysis of ground-calibration data from the ACIS back-illuminated (BI) CCDs (which include S3) showed well before launch that these devices exhibit significant charge transfer inefficiency (CTI). CTI occurs during both parallel and serial transfers, but it is mild enough that the energy resolution is not position-dependent. However, the gain, quantum efficiency, and grade distribution change subtly across the device. In an attempt to mitigate the effects of CTI, Townsley et al. (2001b) have developed a software tool for correcting CTI through a forward-modeling algorithm incorporating a detailed physical CCD model (Townsley et al. 2001a). This model has been tuned using an extensive library of on-orbit calibration data and tested on astrophysical sources. CTI-corrected data require redistribution matrix files (rmfs) and quantum efficiency uniformity (qeu) files distinct from those distributed by the CXC; these have been made publicly available.[2] CTI correcting ACIS-S3 data allows a single rmf to be used across the whole CCD thus making analysis of extended sources more tractable. In addition, recovering the initial event grades makes grade

---

[2]http://www.astro.psu.edu/users/townsley/cti/

filtering uniform across the CCD, and accounting for the charge lost due to transfers improves the energy resolution of the X-ray spectrum.

After correcting the data for CTI, the spectrum of the nuclear region was extracted in pulse-invariant (PI) format from a $2''$-radius circular cell. The background spectrum was extracted from an annulus centered on the nucleus with an inner radius of $2''.5$ and an outer radius of $4''$. The qeu file for the CTI-corrected data was used to generate an ancillary response file (arf) using the CIAO 2.1 tool mkarf which combines the effective area of the mirrors with the qeu and quantum efficiency file. Using the FTOOL grppha, the data were grouped into bins with at least 15 counts for χ^2 fitting. The data were fit with the X-ray spectral analysis tool XSPEC (Arnaud 1996). As the quantum efficiency calibration below 0.5 keV is uncertain, the counts below this value were ignored. The data above 8.0 keV were also ignored for the reasons described in §3.1.

5.1.2. Basic Spectral Modeling

The data were first fit with a power-law model. Though the fit was statistically acceptable ($\chi^2/\nu = 88.2/81$), the residuals showed systematic effects. In particular, there were positive residuals below 1.0 keV and above 5 keV. Also, the best-fitting photon index, $\Gamma = 0.46 \pm 0.09$, was unusually hard; the typical photon index for a radio-quiet QSO is in the range, $\Gamma = 1.7$–2.3 (e.g., Reeves & Turner 2000; George et al. 2000). As Mrk 231 hosts a starburst ring within $1''$ of its nucleus (Bryant & Scoville 1996; Carilli et al. 1998; Taylor et al. 1999), a plausible additional component to add is a Raymond-Smith thermal plasma (Raymond & Smith 1977). The plasma abundance was initially fixed at solar, a reasonable value for an energetic starburst hosting a luminous QSO. The temperature was constrained to lie within the bounds found for local starbursts by Ptak et al. (1999), $kT = 0.2$–3.0 keV. Compared to the simple power law, this model was preferred at the $> 95\%$ confidence level according to the F-test ($\Delta\chi^2 = -7.8$ for two additional fit parameters). For the thermal plasma, the temperature, $kT = 1.1^{+>1.9}_{-0.2}$ keV, although poorly constrained, is consistent with that previously found by Iwasawa (1999). However, the photon index remained atypically flat, $\Gamma = 0.31^{+0.11}_{-0.20}$. Allowing the abun-

dances to vary did not substantially improve the fit ($\Delta\chi^2 = 1.1$), and the best-fitting abundances were poorly constrained and low, $Z = 0.32^{+0.63}_{-0.32} Z_\odot$. As the model fitting was not very sensitive to this parameter and the best-fitting values appear to be unreliable, the abundances were fixed to the solar values for the remainder of the analysis.

Intrinsic absorption can often masquerade as a flattening of the power-law photon index, and so intrinsic absorption was added to the power-law component. This did not improve the fit ($\chi^2/\nu = 80.5/78$), and the best-fitting intrinsic column density was negligible. The photon index remained at an unusually flat value, $\Gamma \approx 0.3$. To push this physical picture further, the photon index was constrained to lie in a reasonable range for radio-quiet QSOs, $\Gamma = 1.5$–2.5. The model fit for Γ "pegged" at the lower bound of 1.5 with $\chi^2/\nu = 121.2/78$. Two additional absorption models were also tested, partial-covering and ionized absorption (Done et al. 1992; Magdziarz & Zdziarski 1995), with the photon index constrained as for the previous example. In both cases, the fits were statistically worse than the simple power law plus thermal plasma, $\chi^2/\nu = 92.5/77$ and $\chi^2/\nu = 103.5/77$, respectively, and the photon index value pegged at $\Gamma = 1.5$. In addition, the models underfit the flux at energies $\gtrsim 5$ keV.

5.1.3. Reflection-Dominated Spectrum and Iron Line

Following the results of Maloney & Reynolds (2000), we next tried fitting a thermal plasma plus a power law reflected from neutral material. Reflected spectra are commonly seen in Seyfert 1 galaxies in addition to the primary power-law component; the latter contributes the majority of the flux in the *Chandra* band. The reflected component is physically understood to arise from the direct X-ray continuum illuminating a Compton-thick accretion disk or molecular torus. In Compton-thick Seyfert 2 galaxies, which are viewed along a line of sight through the putative torus, the primary continuum is completely absorbed. Therefore, reflection dominates the emission.

The XSPEC reflection model, pexrav (Magdziarz & Zdziarski 1995), was used to fit the observed data. Input parameters to this model include

the inclination (i) and abundances of the reflecting medium, as well as the photon index and cutoff energy (E_c) of the illuminating power-law spectrum. The photon index was allowed to vary, but the other parameters were set to the default values in order to reduce the number of free parameters: $\cos(i) = 0.45$, $Z = Z_\odot$, and $E_c = 100$ keV. The model was statistically acceptable, $\chi^2/\nu = 83.7/78$. The best-fitting value and errors for the reflection scaling factor, $R = 5737^{+>10\,000}_{-2637}$, suggest that reflection is dominating the spectrum with essentially no direct continuum reaching the observer. Setting R to produce a pure reflection spectrum gives consistent values for the photon index and the Raymond-Smith temperature.

The best-fitting photon index, $\Gamma = 2.52^{+0.28}_{-0.30}$, though closer to the typical values for radio-quiet QSOs than those given by the fits to a simple power-law model, is unusually high. Based on the *ASCA* correlation for radio-quiet QSOs between Γ and the $\text{FWHM}_{H\beta}$, a photon index of ~ 2.1 for Mrk 231 would be more typical (Reeves & Turner 2000). In addition to the unusually steep photon index, the lack of strong Fe Kα line emission accompanying a reflected continuum is also striking. Adding an unresolved Fe Kα line with $E = 6.4$ keV and $\sigma = 0.01$ keV to the best-fitting model only decreased χ^2 by 0.2. Maloney & Reynolds (2000) measured the Fe Kα equivalent width to be $\text{EW} = 290^{+190}_{-170}$ eV; however, we do not detect an Fe Kα line at 6.4 keV with high statistical significance. Our 90% confidence upper limit on the equivalent width ($\text{EW} < 188$ eV), within the errors of the Maloney & Reynolds (2000) value, is much lower than would be expected with a reflection-dominated model ($\text{EW} \sim 1$–2 keV; e.g., Matt et al. 1996).

Our detection of significant variability above 2 keV is inconsistent with the proposed model of Maloney & Reynolds (2000) for the nucleus where the reflecting medium is the torus, and any scattering medium is on even larger size scales (see their Figure 3). Both of these structures, capable of redirecting X-rays from the nucleus into the line of sight, are on physical scales too large for the observed short-term variability. In any case the reflected component would be unlikely to have energy-dependent variability. No absorption of the reflected component is required; therefore, the reflected component would be unlikely to only exhibit variability above 2 keV as it dominates the flux below 2 keV as well. Since the reflected component is an unlikely source of the observed variability, adding a third component, in addition to the Raymond-Smith plasma and the reflection-dominated continuum, is thus justified. For the spectrum of this third component, we chose an absorbed power law; adding absorption is motivated by the requirement that this component not dominate the flux at the lowest energies for consistency with the observed hard-band variability.

For this fit, the photon indices for both the power-law component and the incident spectrum on the reflecting medium were fixed at $\Gamma = 2.1$ according to the correlation of Reeves & Turner (2000). Given the quality of the data, this was necessary in order to obtain meaningful constraints on the other model parameters. The free parameters of interest were then the Raymond-Smith plasma temperature, the intrinsic absorption column density of the power-law continuum, and the reflection scaling factor of the reflection component. This fit gave a value of $\chi^2/\nu = 69.0/77$, a significant improvement at the $> 95\%$ confidence level over all of the previous models. The Raymond-Smith temperature, $kT = 1.1^{+1.1}_{-0.1}$ keV, was consistent throughout all of the model fits; the bump in the spectrum at ~ 1 keV corresponds to strong Fe L shell emission expected from a plasma of this temperature. The reflection scaling factor, $R = 697^{+427}_{-223}$, remained large. This factor is very sensitive to the data below 1 keV; a higher normalization for the Raymond-Smith plasma component or an additional starburst component at lower temperature would push the reflection scaling factor to higher values corresponding to a completely reflection-dominated spectrum. The value for the best-fitting column density of the power-law component, $N_H = (2.1^{+1.3}_{-0.9}) \times 10^{22}$ cm^{-2}, effectively eliminates flux from the power-law component at energies $\lesssim 2$ keV.

In summary, we find that a three-component model provides a statistically acceptable fit to the observed nuclear spectrum. This complex model is comprised of a Raymond-Smith plasma with $kT \approx 1.1$ keV, an unabsorbed reflection-dominated continuum, plus an absorbed power law with $N_H = (2.9^{+2.5}_{-1.0}) \times 10^{22}$ cm^{-2}. Though this composite model provided a good match to the

observed spectrum (see Figure 9a), it has three significant physical problems. First, the strength of the absorbed power law in this model is not sufficient to dilute the EW of the strong Fe Kα line expected from the reflected component to the observed upper limit, EW < 188 eV. In this model, the absorbed power law contributes $\sim 20\%$ of the observed flux at 6.4 keV. Manually increasing the normalization of the absorbed power-law component to provide the necessary dilution near 6.4 keV results in a continuum spectrum inconsistent with these data. Secondly, the absorbed power law does not provide enough flux above 2 keV to explain the observed amplitude of hard-band variability (see Figure 9b). Finally, the variability time scale implies a physical size of $\sim 10^{15}$ cm for the emitting medium, much smaller than any plausible reflecting medium such as the BAL wind or a molecular torus.

5.1.4. Alternate Model

Mrk 231 exhibits complex frequency-dependent optical and ultraviolet polarization that has been attributed to scattering by dusty clouds (e.g., Goodrich & Miller 1994). The nuclear continuum polarization rises with decreasing wavelength and may approach values as high as 20% in the near ultraviolet (Smith et al. 1995). The absorption and emission-line polarization is highly structured, and Smith et al. (1995) used three separate scattering media to explain the behavior of the polarization position angle. Given this evidence that scattering is an important mechanism contributing to the optical and ultraviolet emission, we considered that a similar situation may be present in the X-rays. Following this reasoning, we examined the possibility that the flat X-ray spectrum is the sum of multiple scattered power-law components with different absorption column densities along each line of sight. This combination could reproduce the unusually flat X-ray spectrum without requiring a large contribution from a reflection-dominated continuum.

Assuming $\Gamma = 2.1$ as in §5.1.3, a minimum of three separate power laws, with column densities of $N_{\mathrm{H}} = 10^{21.1}, 10^{22.5}$, and $10^{23.8}$ cm^{-2}, are required for an acceptable fit to the data ($\Delta\chi^2/\nu = 66.0/75$). The best-fitting temperature for the Raymond-Smith plasma component is consistent to within errors with the previous models. In this

scenario, the second power law dominates the flux between ~ 1.5–5 keV (see Figure 9d), the energy regime contributing most significantly to the observed variability. This model has a slightly lower value of reduced χ^2 compared to the reflection-dominated plus absorbed power-law model, but the improvement is not statistically conclusive. Though speculative, this model can provide an explanation for both the hard-band variability and the lack of a strong Fe Kα emission line if the scattering medium is highly ionized. This model will be discussed and developed further in §6.1.2.

5.1.5. A Jet Contribution to the X-ray Flux?

For completeness, we have also considered other possible contributions to the X-ray flux. As mentioned in §1, a parsec-scale radio jet was detected in Mrk 231 (Ulvestad et al. 1999) with apparent speed, $\beta_{\mathrm{app}} \sim 0.14$. The radio flux of the mas components was found to be variable with a maximum flux density of 60 mJy (Ulvestad et al. 1999). We investigated the possibility that this small-scale radio jet could contribute to the X-ray flux in the *Chandra* spectrum by estimating the synchrotron-self Compton (SSC) flux expected from the total radio flux density (0.1 Jy) of the nucleus. From the jet-to-counterjet ratio (> 45), Ulvestad et al. (1999) estimate $\beta \gtrsim 0.48$ and $\theta \lesssim 10°$ if relativistic boosting is responsible for the one-sided radio structure of the source; though these authors favor free-free absorption as the cause of the one-sided structure, the relativistic boosting scenario would generate the largest jet contribution to the X-ray flux. Assuming $\beta = 0.48$ and $\theta = 10°$, the estimated SSC flux from 0.5–8.0 keV (using eq. 1 from Ghisellini et al. 1993) is $\sim 10^{-22}$ erg cm^{-2} s^{-1}, many orders of magnitude lower than the observed *Chandra* flux (see Table 1). Therefore, SSC emission cannot explain observed X-ray properties.

Another possible source of X-rays from the jet is synchrotron emission. Applying the X-ray-to-radio flux density ratios, $F_{1\ \mathrm{keV}}/F_{15\ \mathrm{GHz}}$, for the knots in the jet of M87 (Biretta et al. 1991; Marshall et al. 2001), we obtained the predicted range of X-ray fluxes for Mrk 231, $F_{1\ \mathrm{keV}} = (0.3$–$9.4) \times 10^{-5}$ photon cm^{-2} s^{-1} keV^{-1}. Though this encompasses the X-ray flux density that we observe, $F_{1\ \mathrm{keV}} \approx 2 \times 10^{-5}$ photon cm^{-2} s^{-1} keV^{-1}, the steep slope, $\Gamma \sim 2.5$ (Marshall et al. 2001), observed for the knots in M87 is inconsistent with

these data ($\Gamma \sim 0.5$). Therefore, X-ray emission from the jet is unlikely to contribute significantly to the observed flux in X-rays.

5.1.6. Spectral Checks

The HRMA preferentially scatters higher energy photons to larger radii. Since the spectrum of the nucleus is so hard, our analysis was also performed on a spectrum extracted from a $3''$ radius aperture with background from an annulus with an inner radius of $3''.5$ and an outer radius of $5''$. This source aperture captures more than 90% of the encircled energy at 6.4 keV. The results from fitting the nuclear emission were consistent with those above, though the soft, thermal emission was not as well constrained. The larger aperture includes more of the extended starburst emission, and so this result is not surprising as the thermal starburst emission from the larger region is unlikely to have a single temperature.

To investigate further the effects of pile-up on our results, the nuclear spectrum was also fit with the simulator-based fitting tool LYNX (Chartas et al. 2000). LYNX utilizes XSPEC (Arnaud 1996) to generate the incident spectrum, the PSF simulator MARX (Wise et al. 1997) to simulate the mirror response, and the Penn State ACIS simulator (Townsley et al. 2001a) to propagate X-rays through the detector. The χ^2 statistic between the simulated and observed spectra is minimized to obtain the best-fitting input model parameters. For this analysis, we used model 4 of Table 2, but similar results would have been obtained other statistically acceptable models. To simulate a spectrum without pile-up, we propagated the best-fitting incident model through LYNX allowing only one incident photon per frame. From this analysis, the average pile-up fraction for the observation is estimated to be 7.7%. For a simple power-law fit to our data, pile-up has the effect of flattening the slope slightly: an incident spectrum which would be fit with a photon index of $\Gamma = 0.4 \pm 0.07$ without pile-up would be measured to have $\Gamma = 0.3 \pm 0.08$ with pile-up for our observed count rate. This level of pile-up would cause $\sim 4\%$ error in the flux measurements. This systematic error is much less than the statistical errors, and so pile-up has not significantly affected our spectral analysis.

The final LYNX output file can also be used to estimate the extent to which the wings of the PSF of the nucleus would contaminate the spectrum of the extended galaxy emission (see §5.2). The simulated radial surface brightness profile in the 2–8 keV band is shown in Figure 3b; the nucleus is expected to contribute approximately 6 counts in the soft band and 16 counts in the hard band to the annulus between $3''$ and $25''$. These contributions are negligible.

5.2. Extended Galaxy Emission

From the images presented in §3, emission extending $\sim 25''$ from the nucleus is clearly evident. For the initial spectral fitting of this emission, a spectrum for the entire galaxy was extracted using a circular source cell with a $25''$ radius. The nucleus was excised with a $3''$ radius circle, and the background spectrum was extracted from a region with an inner radius of $40''$ and an outer radius of $65''$. The rmf and arf were generated as described in §5.1.

The extended emission is soft, and the majority of the galaxy is not detected above ~ 2 keV. Therefore, the data were filtered from 0.5–2.0 keV to maintain an adequate signal-to-noise ratio for the spectral fitting. This also eliminates any significant contamination from the nucleus to the spectrum of the extended galaxy (see §5.1.6). As a first model, a Raymond-Smith plasma with solar abundances was fit. The resulting temperature, $kT \approx 0.4$ keV, was reasonable, but the value of $\chi^2/\nu = 143.7/31$ was clearly unacceptable. Substantial positive residuals between 1.0–2.0 keV indicated that an additional component was required, and so a second Raymond-Smith component was added. The new fit was statistically acceptable ($\chi^2/\nu = 37.2/29$). The two temperatures, $kT = 0.30^{+0.07}_{-0.05}$ keV and $kT = 1.07^{+0.22}_{-0.18}$ keV, were also within the range typically seen in starburst galaxies (0.2–3.0 keV; e.g., Ptak et al. 1999). The spectrum of the galaxy fit with this model is presented in Figure 10.

Some additional systematic positive residuals above 1 keV suggested that a power-law component could also fit the data, and so a power law was substituted for the second Raymond-Smith plasma component. The temperature of the Raymond-Smith plasma increased relative to the cooler one in previous fits, $kT = 0.80^{+0.07}_{-0.11}$ keV. The best-fitting photon index for the power law,

$\Gamma = 2.6 \pm 0.7$, was consistent with emission arising from a population of X-ray binaries, the most likely source for such a component. However, the value of $\chi^2/\nu = 40.6/29$ was not a significant improvement over the previous model.

To investigate whether the spectral components were spatially distinct, we divided the extended galaxy into an inner and outer region with roughly equal counts in each annulus. The inner region had an outer radius of $10''$ with the nuclear region excised, and the outer region excluded the inner region. The background regions for both were the same as for the complete region.

Based on the counts in the spectrum, the data from 0.5–3.0 keV were kept for the spectral analysis of the inner region. Briefly, the inner region was fit equally well with either a two-temperature Raymond-Smith plasma or a power law plus Raymond-Smith component. Both fits produced an acceptable value of $\chi^2/\nu = 14/12$ (see Table 2). The spectrum of the outer region showed less hard X-ray emission, and so the data were filtered as for the entire extended region, $0.5 < E < 2.0$ keV. The Raymond-Smith plasma plus power law was slightly preferred over the two-temperature Raymond-Smith plasma ($\Delta\chi^2 = 1.6$ for the same number of degrees of freedom).

6. Discussion

6.1. Mrk 231 as a Broad Absorption Line QSO

6.1.1. Spectroscopic Classification

The definitive classification of Mrk 231 as a BAL QSO has been debated in the literature for almost three decades. The canonical definition of a BAL QSO, as published in Weymann et al. (1991), is based on a conservative measurement of the equivalent width of the C IV resonance absorption line system called the balnicity index (BI). All QSOs with BI > 0 km s^{-1} are considered to be BAL QSOs. Though Mrk 231 is a bright optical source, the large amount of intrinsic reddening in its spectrum renders it relatively faint in the ultraviolet, and a high-quality spectrum of the C IV region is not available in the literature.

A search of the *HST* archive revealed a Faint Object Spectrograph (FOS) calibration spectrum of Mrk 231 taken on 1996 Nov 21 covering the crucial C IV region. This spectrum, displayed in Figure 11 and unpublished to our knowledge, clearly shows absorption blue-shifted from the C IV and N V emission lines, as well as possible Al III and S IV broad absorption. A rough measure of the balnicity index, BI $\gtrsim 600$ km s^{-1}, is a quantitative indicator of the BAL QSO nature of this object. In addition, Mrk 231 fits within the BAL QSO class based on its X-ray properties.

The quantity α_{ox}, the spectral index of a power law defined by the flux densities at rest-frame 3000 Å and 2 keV, is a useful parameter for measuring the X-ray power of a QSO relative to its ultraviolet continuum emission. A large, negative α_{ox} indicates relatively weak soft X-ray emission; the mean value of α_{ox} for radio-quiet QSOs is ≈ -1.48 (e.g., Laor et al. 1997) with a typical range from -1.7 to -1.3 for objects that do not suffer from X-ray absorption (e.g., Brandt, Laor, & Wills 2000). Weakness in soft X-rays is plausibly explained by intrinsic X-ray absorption, which strongly depresses the observed flux at low-to-moderate energies. A strong correlation of large, negative values of α_{ox} with the absorption-line equivalent width of C IV supports this hypothesis (Brandt et al. 2000). As expected, BAL QSOs populate the extreme end of this correlation: they are the weakest soft X-ray sources as well as the QSOs with the most extreme ultraviolet absorption. Recent spectroscopic observations of three AGN with large, negative α_{ox} values and strong C IV absorption, PG 1411+442, PG 1535+547, and the BAL QSO PG 2112+059, found direct evidence of intrinsic X-ray absorption (Brinkmann et al. 1999; Gallagher et al. 2001b).

For comparison with the BAL QSOs of the Brandt et al. (2000) sample, we have measured the equivalent width of the C IV absorption blueward of the expected location of the emission line, EW ≈ 10 Å. Calculating α_{ox} to complete the comparison is a difficult matter in this complicated object. Though the rest-frame 2 keV flux density can be determined from the best-fitting X-ray model, the ultraviolet spectrum suffers from severe extinction. A naïve measurement of α_{ox} from the observed 3000 Å flux density yields $\alpha_{\mathrm{ox}} = -1.72$; however, this can only be considered an upper bound on the value. Correcting for $A_V = 2$ mag (e.g., Boksenberg et al. 1977) using the extinction curves of Sprayberry & Foltz (1992) results

11

in $\alpha_{ox} = -2.08$; this value includes both starburst and scattered flux as well as the reddened nuclear continuum before the reddening correction and is therefore a reasonable lower limit to α_{ox}. Regardless of the exact value of α_{ox}, the strong C IV absorption coupled with weakness in soft X-rays places Mrk 231 at the heavily absorbed end of the Brandt et al. (2000) correlation, which is populated primarily by BAL QSOs.[3]

6.1.2. X-ray Variability and Spectral Results

With this *Chandra* observation, we can demonstrate convincingly that the 2–8 keV X-ray luminosity is dominated by the unresolved active nucleus in Mrk 231. The hard-band radial profile is consistent with the *Chandra* PSF, and the significant, hard-band variability provides compelling evidence that *Chandra* is probing within light hours of the central black hole. At the observed rate the flux would decrease by a factor of 2 in ≈ 7 hr. The $45 \pm 14\%$ decrease in count rate in the hard band represents a luminosity difference, $\Delta L_X \approx 10^{42}$ erg s^{-1}; variability of this magnitude can only reasonably originate in the immediate vicinity of the active nucleus. In addition, the compact spatial extent and very hard spectrum of the dominant energy source preclude a significant contribution by thermal starburst emission. As an alternative, a concentrated population of ultraluminous X-ray binaries cannot reasonably reproduce the variability, the spectrum, or the luminosity in the 2.0–8.0 keV band, $L_{2-8} = 10^{42.2}$ erg s^{-1}.

The measured range of α_{ox}, $-2.08 < \alpha_{ox} < -1.72$, suggests a source that is under-luminous in the X-ray band by a factor of 6–36, and absorption remains the most likely explanation for this faintness. Though the moderate signal-to-noise ratio of these data is not sufficient to convincingly constrain the multi-component spectral properties of Mrk 231, progress has been made. Assuming a single, direct, highly absorbed continuum as the sole source of the nuclear X-rays would require a bizarre and contrived absorber in order to force the model to match the observed flatness of the X-ray spectrum (see §5.1.2). Though a reflection-

dominated model such as that examined by Maloney & Reynolds (2000) remains feasible based on the spectral fitting alone, our detection of significant variability is inconsistent with their physical picture. The observed X-ray variability during the *Chandra* observation strongly suggests that continuum emitted on small scales is contributing significantly to the hard-band flux. This continuum cannot reasonably be considered to be direct as the X-ray flux is not sufficient for this luminous QSO, and so we prefer an indirect (i.e., reflected or scattered) origin for this variable component.

For a physically reasonable reflecting medium, the size scale is too large to account for the short observed time scale of the variability. The smallest possible source of a reflecting medium would be the BAL wind (e.g., Elvis 2000) at distances typical of the Broad Line Region (e.g., Ogle 1998). Even if the BAL wind resides at the smallest radii modeled ($R \sim 10^{16}$ cm; e.g., Murray et al. 1995), however, the shortest expected time scale of variability for the reflected continuum would be days to weeks as opposed to the hours observed. Therefore, even assuming the smallest reasonable scale for reflecting material, a reflection-dominated continuum is not favored by our observation of hard-band variability.

Our alternate model for the nuclear continuum is comprised of three scattered power-law spectra absorbed by different column densities of gas, and this model also provides a statistically acceptable fit to the data. We interpret these three power-law components as scattered rather than direct based on luminosity arguments; after correcting for absorption, none of them could provide the 2–10 keV X-ray luminosity of $L_X \gtrsim 10^{44}$ erg s^{-1} expected from the infrared power (e.g., Risaliti et al. 2000). The short time scale of the variability provides a spatial scale for at least one of the scattering regions of $R \lesssim 10^{15}$ cm. An electron mirror Thomson scattering X-rays would require densities of $n \gtrsim 10^9$ cm^{-3} on these small scales (assuming a Thomson optical depth of 0.5). Given the implied X-ray luminosity, particle density, and size, the ionization state of this gas can be estimated: $\xi = L_X/(nR^2) \sim 10^5$ erg cm s^{-1}.

This scenario supplies a coherent explanation for the hard-band variability as well as the lack of detected Fe Kα emission. The variability above ~ 2 keV can be explained by flux changes of a

---

[3]Though Brandt et al. (2000) did not correct for intrinsic reddening in their ultraviolet measurements, several of the BAL QSOs in their sample, e.g., PG 2112+059, do not have reddened continua. Those that do, such as PG 1700+518, would only have more negative values of α_{ox}.

single component, a scattered power law with intrinsic absorption of $N_H = 10^{22.5}$ cm^{-2}. Strong Fe Kα line emission would not be expected from scattering off of a highly ionized plasma ($\xi \sim 10^5$ erg cm s^{-1}) where the Fe atoms are largely stripped of electrons (Kallman & Bautista 2001).

Our lack of detection of any direct component to the top of the *Chandra* band-pass supports the conclusion of Maloney & Reynolds (2000) that an intrinsic absorber with a Compton-thick column density of $\gtrsim 10^{24}$ cm^{-2} blocks these X-rays. Furthermore, for a reasonable geometry, the blockage of the direct emission combined with the presence of the scattered emission implies that the Compton-thick absorber is on a roughly similar scale to the scattering mirror; absorbers much larger than the mirror would see it as a point source and would thus block it entirely (see Figure 12 for a possible structure). Given the small scales implied for this absorber as well as the requisite column density, this absorber could be identified with the "hitchhiking gas" proposed by Murray et al. (1995), which shields the BAL wind from becoming completely ionized by extreme ultraviolet and soft X-ray photons. The hitchhiking gas would not contribute a reflected continuum because it is so highly ionized, though it could scatter X-rays into the line of sight. Thus the hitchhiking gas could provide both the Compton-thick absorber along the direct line of sight and the small-scale scattering medium that preserves short timescale variability.

For the absorbers of the multiple scattered power laws, the BAL wind is a reasonable candidate. As mentioned above, radiative acceleration models put the BAL wind on much larger scales ($\gtrsim 10^{16}$ cm^{-2}) than our proposed scatterer, and the column densities for this wind are expected to be $\sim 10^{23}$ cm^{-2} (Proga et al. 2000). This column density is similar to the X-ray column densities measured for BAL QSOs from X-ray spectroscopy (Mathur et al. 2001; Green et al. 2001; Gallagher et al. 2001a), as well as the column densities of two of the three scattered power-law components in our modeling. Multi-epoch observations of Mrk 231 are certainly required to investigate the possibility of multiple scattered components further. These individual absorbed power-law components might be expected to vary with time delays dependent on the physical locations

of their scattering media; in this case, flux variations in the different energy bands < 1.5 keV, 1.5–5 keV, and > 5 keV would provide additional support for this proposed model.

Based on *ROSAT* data, Boller, Brandt, & Fink (1996) and Laor et al. (1997) found a significant correlation between the X-ray photon indices of radio-quiet AGN and the value for the FWHM$_{H\beta}$, where those AGN with the narrowest broad Balmer lines, Narrow-Line Seyfert 1 galaxies (NLS1s), tended toward the steep end of the distribution of Γ. Subsequent work with *ASCA* in the 2–10 keV band has extended this finding to higher energy, although the spread of Γ in the 2–10 keV band is much smaller (e.g., Brandt, Mathur, & Elvis 1997; Reeves & Turner 2000). Mrk 231 has relatively narrow Balmer emission lines, FWHM$_{H\alpha} = 2870$ km s^{-1} (Boroson & Meyers 1992) and FWHM$_{H\beta} = 3000$ km s^{-1} (Lípari et al. 1993), particularly for a QSO of its luminosity. As a low-ionization BAL QSO, Mrk 231 shares several spectral characteristics with NLS1s such as weak [O III] lines and strong optical Fe II emission. This similarity suggests a physical link between the low-ionization BAL QSOs and the NLS1s; perhaps both populations are radiating at a higher fraction of the Eddington luminosity (e.g., Brandt & Gallagher 2000). In order to pursue this potential link, a direct measurement of the underlying photon index of a low-ionization BAL QSO would offer powerful evidence for a connection. Unfortunately, with these data and the evident complexity of the X-ray spectrum, we are not able to constrain the underlying photon index of the X-ray spectrum. The extreme X-ray faintness of other low-ionization BAL QSOs (e.g., Gallagher et al. 1999; Green et al. 2001) may prevent a direct measurement of Γ in these objects for many years. The complexity we have found in the spectrum of Mrk 231 should be remembered when interpreting X-ray data on more distant (and therefore fainter and unresolved) low-ionization BAL QSOs.

6.2. Mrk 231 as a Starburst Galaxy

In this observation of Mrk 231, *Chandra* has resolved the extent and structure of an X-ray luminous starburst. Over the entire galaxy, the 0.5–2.0 keV luminosity, $L_{0.5-2.0}$, equals $10^{41.2}$ erg s^{-1}, with $\sim 30\%$ from the inner $2''$ (1.6 kpc). The strong Fe L shell emission of the nuclear spectrum

provides evidence for a ~ 1 keV thermal component in addition to the non-thermal spectrum. This thermal X-ray component supports the radio evidence for star formation in the subkiloparsec gas disk (Carilli et al. 1998). In this disk, the star-formation rate claimed by Taylor et al. (1999) based on their radio observations is 220 $M_\odot$ yr^{-1}. Such an active starburst region might be expected to be more X-ray luminous; M82 has an 0.5–2.0 keV luminosity of $\sim 10^{40.7}$ erg s^{-1} with a star-formation rate an order of magnitude lower (e.g., Ptak et al. 1997). Though its total flux from star formation places Mrk 231 at the X-ray luminous end of the starburst population, it is still about an order of magnitude fainter from 0.5–2.0 keV than the most X-ray luminous starburst, NGC 3256 (Moran et al. 1999). The starburst emission certainly has more than one component, though discriminating between a two-temperature thermal plasma and a thermal plasma plus power-law model is not possible at present. The temperature of the thermal plasma within the nuclear region is ~ 1 keV, and the data are consistent with such a component contributing at all radii in the galaxy. However, the best-fitting plasma temperature at a given radius should only be considered an emission-measure-weighted average as the actual X-ray spectrum is likely to be complex. Higher counting statistics and better low-energy calibration of ACIS-S3 below 0.5 keV would contribute significantly to understanding the distribution of hot gas in this starburst in more detail.

The one possible off-nuclear source is consistent with the luminous point sources seen in other starburst galaxies. One source hardly characterizes a population, however, and further observations would allow a more definitive description of the luminous X-ray binary population of this galaxy.

7. Future Work

Mrk 231 was the first example of a low-ionization BAL QSO with X-ray spectroscopy, and it may be one of very few for many years as this class populates the X-ray faintest end of the BAL QSO distribution (Green et al. 2001). From X-ray spectroscopy of the handful of BAL QSOs bright enough for such analysis, the typical BAL QSO spectrum appears to be a normal QSO continuum absorbed by gas with column densities of $N_{\rm H} = 10^{22-23.5}$ cm^{-2} (e.g., Gallagher et al. 2001a,b; Green et al. 2001). Mrk 231 does not fit within this paradigm as it appears to have Compton-thick obscuration with only indirect X-ray reaching the observer. If Mrk 231 is typical of the class of low-ionization BAL QSOs, their extreme faintness may result from similar spectra. Spectra such as that exhibited by Mrk 231, whether reflection-dominated or composed of several, absorbed power laws, are much fainter than a direct, absorbed continuum and have a fundamentally different spectral shape. Though spectroscopy of other objects may be difficult, a statistical comparison of the hardness ratios of low-ionization BAL QSOs and normal BAL QSOs can investigate this hypothesis.

Furthermore, Mrk 231 is likely to be the only host galaxy of a BAL QSO imaged in X-rays for many years; BAL QSOs tend to lie at much greater distances. For comparison, IRAS 07598+6508, the next nearest known BAL QSO, has a redshift of $z = 0.149$. Even with relatively good quality data and the advantage of excellent spatial resolution, the X-ray data for Mrk 231 are complex; similar spectra from unresolved sources at higher redshifts may prove intractable and must be treated with great care. Additional observations of Mrk 231 with *Chandra* to increase the signal-to-noise ratio for both the extended galaxy and nuclear spectra would allow for study of variability on longer time scales where the amplitude of variability may well be larger and could correlate with observed changes over time in the BALs.

Mrk 231 has been put forth as a possible local example of energetic starburst/QSO phenomena common in the early Universe. It would be interesting to examine the hardness ratio and flux evolution as a function of redshift of such a galaxy for comparison with sources found in deep X-ray surveys. At present however, the spectrum above 8 keV is highly uncertain, thus making such analysis above $z \approx 1$ speculative. The question of the true power of this QSO remains, and the far-infrared and hard X-rays are the most likely regimes for addressing this issue. There was no OSSE detection of Mrk 231 (Dermer et al. 1997); however, this limit is not very sensitive. An 80 ks observation with the Phoswich Detection System (15–300 keV) on *Beppo-SAX* scheduled for Cycle 5 should provide significant insight into the true

power in the hard X-ray regime, and further information on whether the direct continuum is beginning to show through at the hard end of the ACIS bandpass.

REFERENCES

Adams, T. F., & Weedman, D. W. 1972, ApJ, 173, L109

Arakelian, M. A., Dibay, E. A., & Esipov, V. F. 1971, Astrofizika, 7, 177

Arnaud, K. A. 1996, in ASP Conf. Ser. 101, Astronomical Data Analysis Software and Systems V, ed. G. Jacoby & J. Barnes (San Francisco: ASP), 17

Bauer, F. E., Brandt, W. N., Sambruna, R. M., Chartas, G., Garmire, G. P., Kaspi, S., & Netzer, H. 2001, AJ, 122, 182

Biretta, J. A., Stern, C. P., & Harris, D. E. 1991, AJ, 101, 1632

Boksenberg, A., Carswell, R. F., Allen, D. A., Fosbury, R. A. E., Penston, M. V., & Sargent, W. L. W. 1977, MNRAS, 178, 451

Boller, T., Brandt, W. N., & Fink, H. 1996, A&A, 305, 53

Boroson, T. A., & Meyers, K. A. 1992, ApJ, 397, 442

Boroson, T. A., Meyers, K. A., Morris, S. L., & Persson, S. E. 1991, ApJ, 370, L19

Brandt, W. N., & Gallagher, S. C. 2000, New Astronomy Review, 44, 461

Brandt, W. N., Laor, A., & Wills, B. J. 2000, ApJ, 528, 637

Brandt, W. N., Mathur, S., & Elvis, M. 1997, MNRAS, 285, L25

Brinkmann, W., Wang, T., Matsuoka, M., & Yuan, W. 1999, A&A, 345, 43

Bryant, P. M., & Scoville, N. Z. 1996, ApJ, 457, 678

Carilli, C. L., Wrobel, J. M., & Ulvestad, J. S. 1998, AJ, 115, 928

Chartas, G., Gupta, V., Garmire, G., Jones, C., Falco, E. E., Shapiro, I. I., & Tavecchio, F. 2002, ApJ, in press (astro-ph/0108277)

Chartas, G., et al. 2000, ApJ, 542, 655

Cutri, R. M., Rieke, G. H., & Lebofsky, M. J. 1984, ApJ, 287, 566

Dermer, C. D., Bland-Hawthorn, J., Chiang, J., & McNaron-Brown, K. 1997, ApJ, 484, L121

Done, C., Mulchaey, J. S., Mushotzky, R. F., & Arnaud, K. A. 1992, ApJ, 395, 275

Downes, D., & Solomon, P. M. 1998, ApJ, 507, 615

Eales, S. A., & Arnaud, K. A. 1988, ApJ, 324, 193

Ebeling, H., White, D. A., & Rangarajan, F. V. N. 2001, MNRAS, submitted

Elvis, M. 2000, ApJ, 545, 63

Elvis, M., Lockman, F. J., & Wilkes, B. J. 1989, AJ, 97, 777

Forster, K., Rich, R. M., & McCarthy, J. K. 1995, ApJ, 450, 74

Gallagher, S. C., Brandt, W. N., Chartas, G., & Garmire, G. P. 2001a, ApJ, accepted

Gallagher, S. C., Brandt, W. N., Laor, A., Elvis, M., Mathur, S., Wills, B. J., & Iyomoto, N. 2001b, ApJ, 546, 795

Gallagher, S. C., Brandt, W. N., Sambruna, R. M., Mathur, S., & Yamasaki, N. 1999, ApJ, 519, 549

Gehrels, N. 1986, ApJ, 303, 336

George, I. M., Turner, T. J., Yaqoob, T., Netzer, H., Laor, A., Mushotzky, R. F., Nandra, K., & Takahashi, T. 2000, ApJ, 531, 52

Ghisellini, G., Padovani, P., Celotti, A., & Maraschi, L. 1993, ApJ, 407, 65

Goldader, J. D., Joseph, R. D., Doyon, R., & Sanders, D. B. 1995, ApJ, 444, 97

Goodrich, R. W., & Miller, J. S. 1994, ApJ, 434, 82

Green, P. J., Aldcroft, T. L., Mathur, S., Wilkes, B. J., & Elvis, M. 2001, ApJ, in press (astro-ph/0105258)

Hamilton, D., & Keel, W. C. 1987, ApJ, 321, 211

Hutchings, J. B., & Neff, S. G. 1987, AJ, 93, 14

Iwasawa, K. 1999, MNRAS, 302, 96

Kallman, T., & Bautista, M. 2001, ApJS, 133, 221

Kollatschny, W., Dietrich, M., & Hagen, H. 1992, A&A, 264, L5

Krabbe, A., Colina, L., Thatte, N., & Kroker, H. 1997, ApJ, 476, 98

Lai, O., Rouan, D., Rigaut, F., Arsenault, R., & Gendron, E. 1998, A&A, 334, 783

Laor, A., Fiore, F., Elvis, M., Wilkes, B. J., & McDowell, J. C. 1997, ApJ, 477, 93

Lípari, S., Terlevich, R., & Macchetto, F. 1993, ApJ, 406, 451

Low, F. J., Huchra, J. P., Kleinmann, S. G., & Cutri, R. M. 1988, ApJ, 327, L41

Ma, C., et al. 1998, AJ, 116, 516

Magdziarz, P., & Zdziarski, A. A. 1995, MNRAS, 273, 837

Makishima, K., et al. 2000, ApJ, 535, 632

Maloney, P. R., & Reynolds, C. S. 2000, ApJ, 545, L23

Markarian, B. E. 1969, Astrofizika, 5, 286

Marshall, H. L., Miller, B. P., Davis, D. S., Perlman, E. S., Wise, M., Canizares, C. R., & Harris, D. E. 2001, ApJ, in press (astro-ph/0109160

Mathur, S., Matt, G., Green, P. J., Elvis, M., & Singh, K. P. 2001, ApJ, 551, L13

Matt, G., Brandt, W. N., & Fabian, A. C. 1996, MNRAS, 280, 823

Moran, E. C., Lehnert, M. D., & Helfand, D. J. 1999, ApJ, 526, 649

Murray, N., Chiang, J., Grossman, S. A., & Voit, G. M. 1995, ApJ, 451, 498

Ogle, P. M. 1998, Ph.D. thesis, California Institute of Technology

Proga, D., Stone, J. M., & Kallman, T. R. 2000, ApJ, 543, 686

Ptak, A., Serlemitsos, P., Yaqoob, T., & Mushotzky, R. 1999, ApJS, 120, 179

Ptak, A., Serlemitsos, P., Yaqoob, T., Mushotzky, R., & Tsuru, T. 1997, AJ, 113, 1286

Raymond, J. C., & Smith, B. W. 1977, ApJS, 35, 419

Reeves, J. N., & Turner, M. J. L. 2000, MNRAS, 316, 234

Rieke, G. H. 1988, ApJ, 331, L5

Rieke, G. H., & Low, F. J. 1972, ApJ, 176, L95

Rieke, G. H., & Low, F. J. 1975, ApJ, 200, L67

Rigopoulou, D., Lawrence, A., & Rowan-Robinson, M. 1996, MNRAS, 278, 1049

Rigopoulou, D., Spoon, H. W. W., Genzel, R., Lutz, D., Moorwood, A. F. M., & Tran, Q. D. 1999, AJ, 118, 2625

Risaliti, G., Gilli, R., Maiolino, R., & Salvati, M. 2000, A&A, 357, 13

Sanders, D. B., Scoville, N. Z., & Soifer, B. T. 1991, ApJ, 370, 158

Sanders, D. B., Scoville, N. Z., Soifer, B. T., Young, J. S., & Danielson, G. E. 1987, ApJ, 312, L5

Sanders, D. B., Soifer, B. T., Elias, J. H., Neugebauer, G., & Matthews, K. 1988, ApJ, 328, L35

Sanders, J. S., & Fabian, A. C. 2001, MNRAS, 325, 178

Schlegel, E. M. 1995, Reports of Progress in Physics, 58, 1375

Smith, P. S., Schmidt, G. D., Allen, R. G., & Angel, J. R. P. 1995, ApJ, 444, 146

Sprayberry, D., & Foltz, C. B. 1992, ApJ, 390, 39

Surace, J. A., & Sanders, D. B. 1999, ApJ, 512, 162

Surace, J. A., Sanders, D. B., Vacca, W. D., Veilleux, S., & Mazzarella, J. M. 1998, ApJ, 492, 116

Taylor, G. B., Silver, C. S., Ulvestad, J. S., & Carilli, C. L. 1999, ApJ, 519, 185

Townsley, L. K., Broos, P. S., Chartas, G., Moskalenko, E., Nousek, J. A., & Pavlov, G. G. 2001a, Nuclear Instruments & Methods, accepted (astro-ph/0111003)

Townsley, L. K., Broos, P. S., Nousek, J. A., & Garmire, G. P. 2001b, Nuclear Instruments & Methods, accepted (astro-ph/0111031)

Turner, T. J. 1999, ApJ, 511, 142

Ulvestad, J. S., Wrobel, J. M., & Carilli, C. L. 1999, ApJ, 516, 127

Ulvestad, J. S., Wrobel, J. M., Roy, A. L., Wilson, A. S., Falcke, H., & Krichbaum, T. P. 1999, ApJ, 517, L81

Weedman, D. W. 1973, ApJ, 183, 29

Weymann, R. J., Morris, S. L., Foltz, C. B., & Hewett, P. C. 1991, ApJ, 373, 23

Wise, M. W., Huenemoerder, D. P., & Davis, J. E. 1997, in ASP Conf. Ser. 125: Astronomical Data Analysis Software and Systems VI, ed. G. Hunt & H. E. Payne (San Francisco: ASP), 477

TABLE 1
COUNTS, FLUXES, AND LUMINOSITIES

Region[a]	Source Counts	Background Counts[b] (0.5–8.0 keV)	$F_{0.5-2}/F_{2-8}$[c] $(10^{-14}$ erg cm^{-2} s$^{-1})$	$L_{0.5-2}/L_{2-8}$[d] $(10^{40}$ erg s$^{-1})$
Nucleus	1447 ± 38	36 ± 4	$5.4^{+1.1}_{-1.2}/45^{+13}_{-16}$	17.1/153
Diffuse Emission	833 ± 29	240 ± 15	$3.5^{+0.3}_{-0.4}/\cdots$	12/$\cdots$
Inner Region	323 ± 18	36 ± 6	$1.8^{+0.3}_{-0.3}/\cdots$	6.2/$\cdots$
Outer Region	510 ± 23	204 ± 14	$2.1^{+0.6}_{-1.0}/\cdots$	7.3/$\cdots$

[a]Regions are defined in §5.

[b]Counts in the background regions, defined in §5, have been normalized to the areas of the source regions.

[c]The fluxes are calculated from the best-fitting models; see Table 2. Errors are determined from the 90% confidence limits on the absolute normalization of the dominant component.

[d]The luminosities are calculated using $z = 0.042$, $H_0 = 75$ km s^{-1} Mpc^{-1}, and $q_0 = \frac{1}{2}$.

TABLE 2

PARAMETERS FOR MODEL FITS TO THE *Chandra* DATA FOR MRK 231[a]

Model[b]	Γ	Parameter	Values	χ^2/ν	$P(\chi^2|\nu)$[c]
Nucleus					
1. Power law	0.46 ± 0.09	$\cdots$	$\cdots$	88.2/81	0.37
2. Power law and Raymond-Smith plasma[d]	$0.31^{+0.11}_{-0.20}$	kT (keV)	$1.1^{+>1.9}_{-0.2}$	80.4/79	0.44
3. Reflected power law	$2.52^{+0.28}_{-0.30}$	R	$5737^{+>10^4}_{-2637}$	83.7/78	0.31
and Raymond-Smith plasma		kT (keV)	$1.3^{+>1.7}_{-0.6}$		
4. Reflected power law,	2.1[e]	R	697^{+427}_{-223}	69.0/77	0.73
absorbed power law, and	2.1[e]	$N_{\rm H}$ (10^{22} cm^{-2})	$2.1^{+1.3}_{-0.9}$		
Raymond-Smith plasma		kT (keV)	$1.1^{+1.1}_{-0.1}$		
5. Three absorbed power laws and	2.1[e]	$N_{\rm H}$ (10^{22} cm^{-2})	$0.12^{+0.12}_{-0.09}$	66.0/75	0.76
	2.1[e]	$N_{\rm H}$ (10^{22} cm^{-2})	$3.21^{+1.43}_{-1.37}$		
	2.1[e]	$N_{\rm H}$ (10^{22} cm^{-2})	$59.6^{+89.0}_{-33.3}$		
Raymond-Smith plasma		kT (keV)	$1.34^{+>1.67}_{-0.32}$		
Extended Emission, $E < 2.0$ keV					
1. Raymond-Smith plasma		kT (keV)	0.4[e]	143.7/31	$< 10^{-6}$
2. Two-temperature Raymond-Smith plasma		kT (keV)	$0.30^{+0.07}_{-0.05}$	37.2/29	0.14
		kT (keV)	$1.07^{+0.22}_{-0.12}$		
3. Raymond-Smith plasma and power law	$2.58^{+0.66}_{-0.55}$	kT (keV)	$0.80^{+0.07}_{-0.11}$	40.6/29	0.07
Inner Region, $E < 3.0$ keV					
1. Two-temperature Raymond-Smith plasma		kT (keV)	$0.34^{+0.08}_{-0.10}$	13.9/12	0.31
		kT (keV)	$1.21^{+0.41}_{-0.21}$		
2. Raymond-Smith plasma and power law	$2.45^{+0.74}_{-0.59}$	kT (keV)	$0.84^{+0.20}_{-0.05}$	13.6/12	0.32
Outer Region, $E < 2.0$ keV					
1. Two-temperature Raymond-Smith plasma		kT (keV)	$0.26^{+0.12}_{-0.11}$	11.5/14	0.65
		kT (keV)	$0.98^{+0.25}_{-0.23}$		
2. Raymond-Smith plasma and power law	$3.81^{+2.36}_{-1.12}$	kT (keV)	$0.81^{+0.14}_{-0.15}$	9.9/14	0.77

[a]All errors are for 90% confidence taking all parameters to be of interest other than absolute normalization.

[b]All models have fixed Galactic absorption of 1.03×10^{20} cm^{-2}; see §1

[c]The probability, if the given model were correct, that this value of χ^2 or greater would be obtained where ν is the number of degrees of freedom.

Fig. 1.— X-ray images of Mrk 231 adaptively smoothed at the 2.5σ level displayed on a logarithmic scale. The images have been filtered to eliminate the background flare leaving an effective exposure of 37.1 ks. The white cross marks the precise radio coordinates; the X-ray centroids in each band are within 1″ of this position. The contours indicate the 2.5σ significance contours. **(a)** Full-band (0.35–8.0 keV) image. **(b)** Soft-band (0.35–2.0 keV) image. **(c)** Hard-band (2.0–8.0 keV) image.

Fig. 2.— Surface plots of the adaptively smoothed images of Mrk 231 in the **(a)** soft-band (0.35–2.0 keV) and **(b)** hard-band (2.0–8.0 keV). The nuclear region clearly contributes significantly to the emission at all energies, and the comparable peak intensity in each band indicates the unusually hard nature of the point source. Note the extended emission apparent in the soft band that is not seen in the hard band.
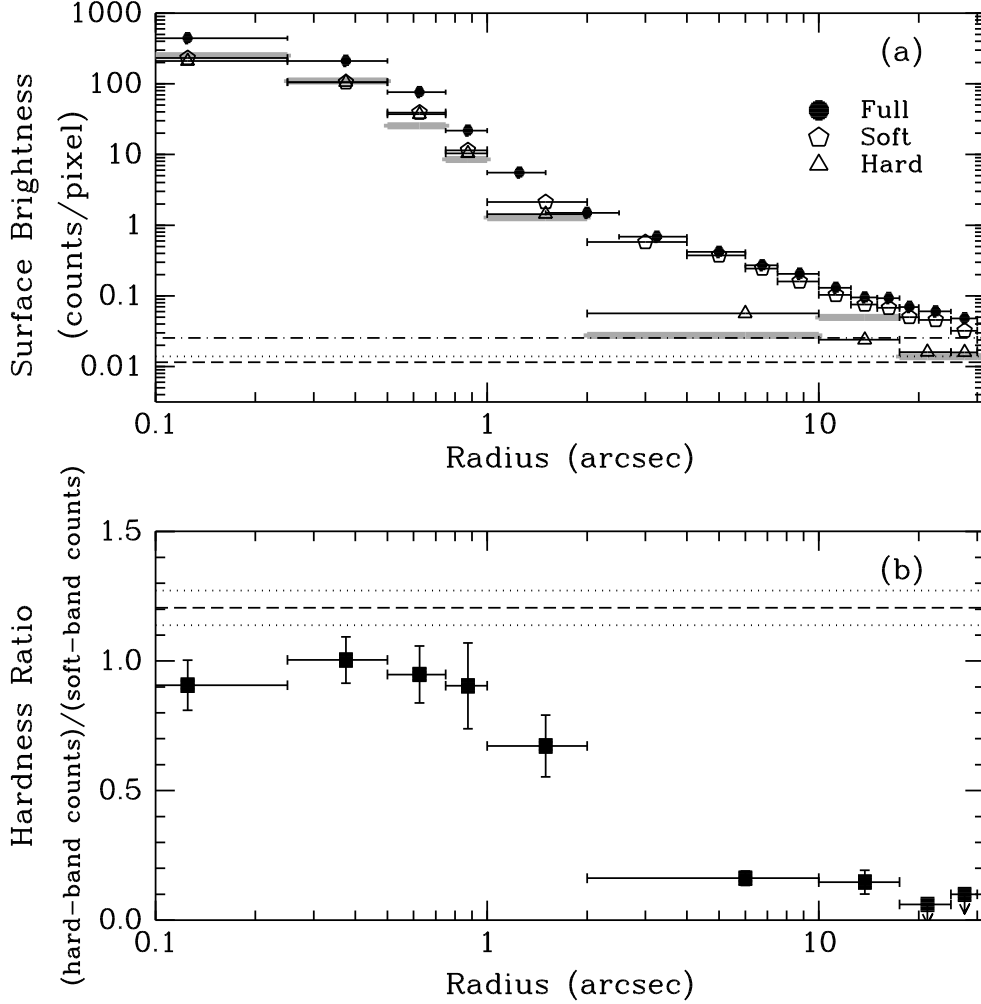
Fig. 3.— **(a)** Radial surface-brightness profiles of the emission from Mrk 231. Each data point is the counts per pixel in an annulus with the average radius marked; the annulus width is indicated by the horizontal error bars. The bin size was chosen so each bin contained at least 50 counts, and the errors in the vertical direction are comparable to the size of the symbols. The filled circles indicate the surface brightness in the full-band image while open pentagons and open triangles show the surface brightness in the soft and hard bands, respectively. The thick, gray line is the simulated surface-brightness profile for the hard band based on modeling with MARX and LYNX (see §5.1.6). The hard-band emission out to 18″ is consistent with the PSF. The dot-dashed, dashed, and dotted lines indicate the surface brightness of the background for the full, soft, and hard bands, respectively. **(b)** Background-subtracted, hardness-ratio profile as a function of radius. The nucleus is significantly harder than the soft extended emission. Vertical error bars include the errors in the hardness ratio as well as the background. Where the hard-band emission is consistent with the background, the calculated hardness ratio is given as an upper limit. The dashed line indicates the hardness ratio of the background outside of the galaxy with the dotted lines showing the errors for that measurement.

Fig. 4.— **(a)** Archival *HST* WFPC2 image taken with the F439W (blue) filter (Surace et al. 1998) overlaid with the contours from the adaptively smoothed, full-band X-ray image. The optical image is displayed with a logarithmic scale, and X-ray contours represent factors of two in counts. The extended structure in the X-rays does not appear to correlate with the crescent-shaped star-forming region to the South of the nucleus evident in the blue image. **(b)** Narrow-band Hα image (Hamilton & Keel 1987) overlaid with the contours from the adaptively smoothed, soft-band X-ray image. The optical image is displayed with a logarithmic scale, and the contours represent factors of two in counts. Note the region of enhanced emission to the Northeast of the nucleus evident in both the full and soft-band X-ray contours.
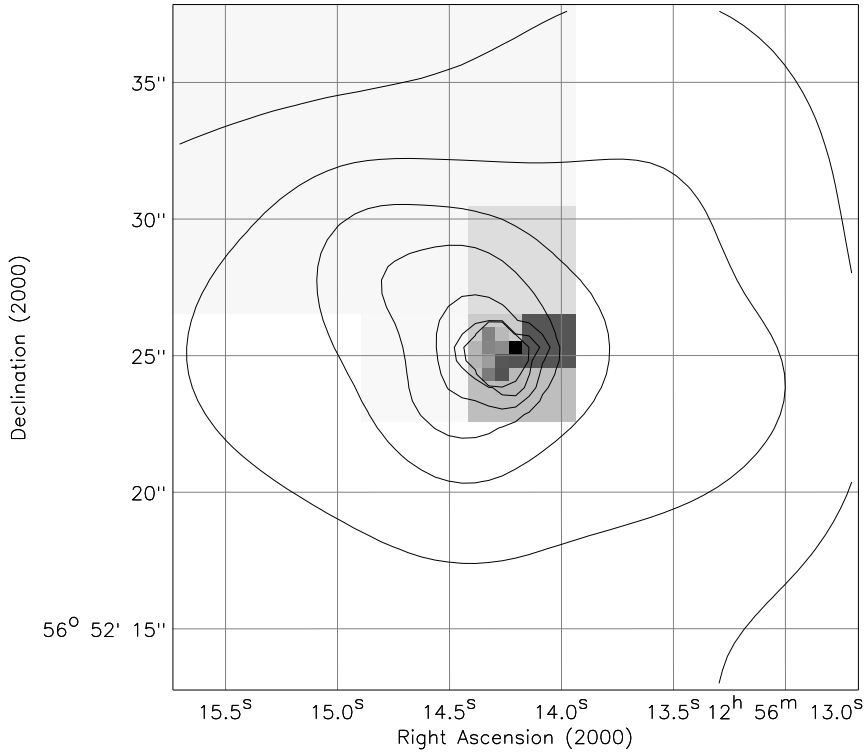
Fig. 5.— Adaptively binned X-ray hardness-ratio map showing the ratio of 2.0–8.0 keV to 0.35–2.0 keV counts displayed with a linear scale; white indicates the softest regions (see §3). Only the region of the galaxy displayed in this figure has sufficient counts after background subtraction to measure the hardness ratio. The nucleus has the highest surface brightness which results in the finest resolution (or smallest pixels) in the map. The galaxy is significantly softer than the nucleus; within the errors, the region at radii $\gtrsim 2''$ from the nucleus has a consistent hardness ratio, $\mathrm{HR_{disk}} \approx 0.1$–$0.2$. Note the hard region to the West of the nucleus spatially coincident with the reddest $B - R$ contours from Hutchings & Neff (1987). The overlaid contours show the intensity from the adaptively smoothed full-band X-ray image. Contour levels represent factors of two in counts.
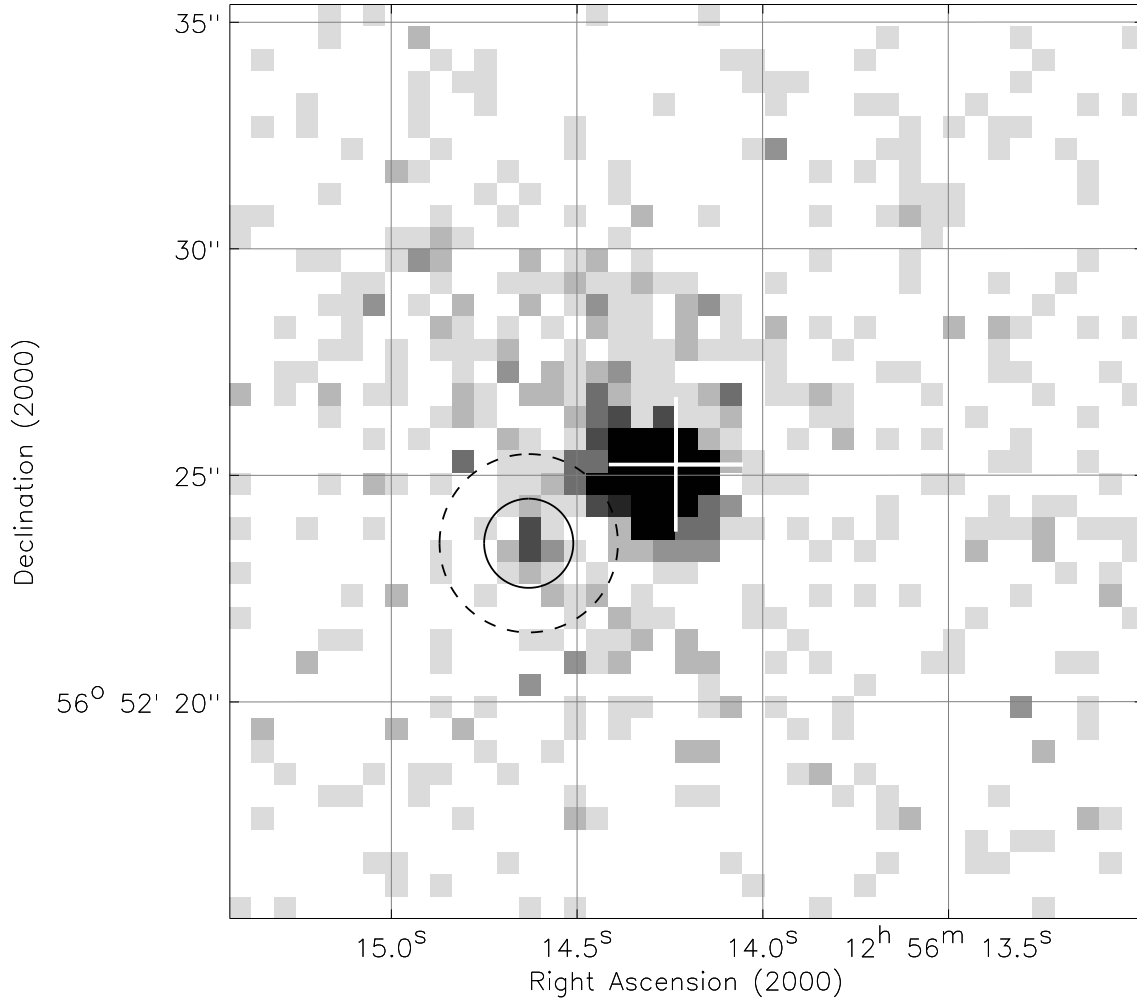
Fig. 6.— Full-band image of the $20'' \times 20''$ region immediately surrounding the nucleus of Mrk 231 displayed with a linear scale. The precise radio coordinates of the nucleus are marked with a white cross, and the putative non-nuclear source, possibly an ultra-luminous X-ray binary or supernova remnant, is enclosed in the concentric black circles. The background region was extracted from the annulus with an outer radius of $2''$ (dashed line) and an inner radius of $1''$ (solid line).
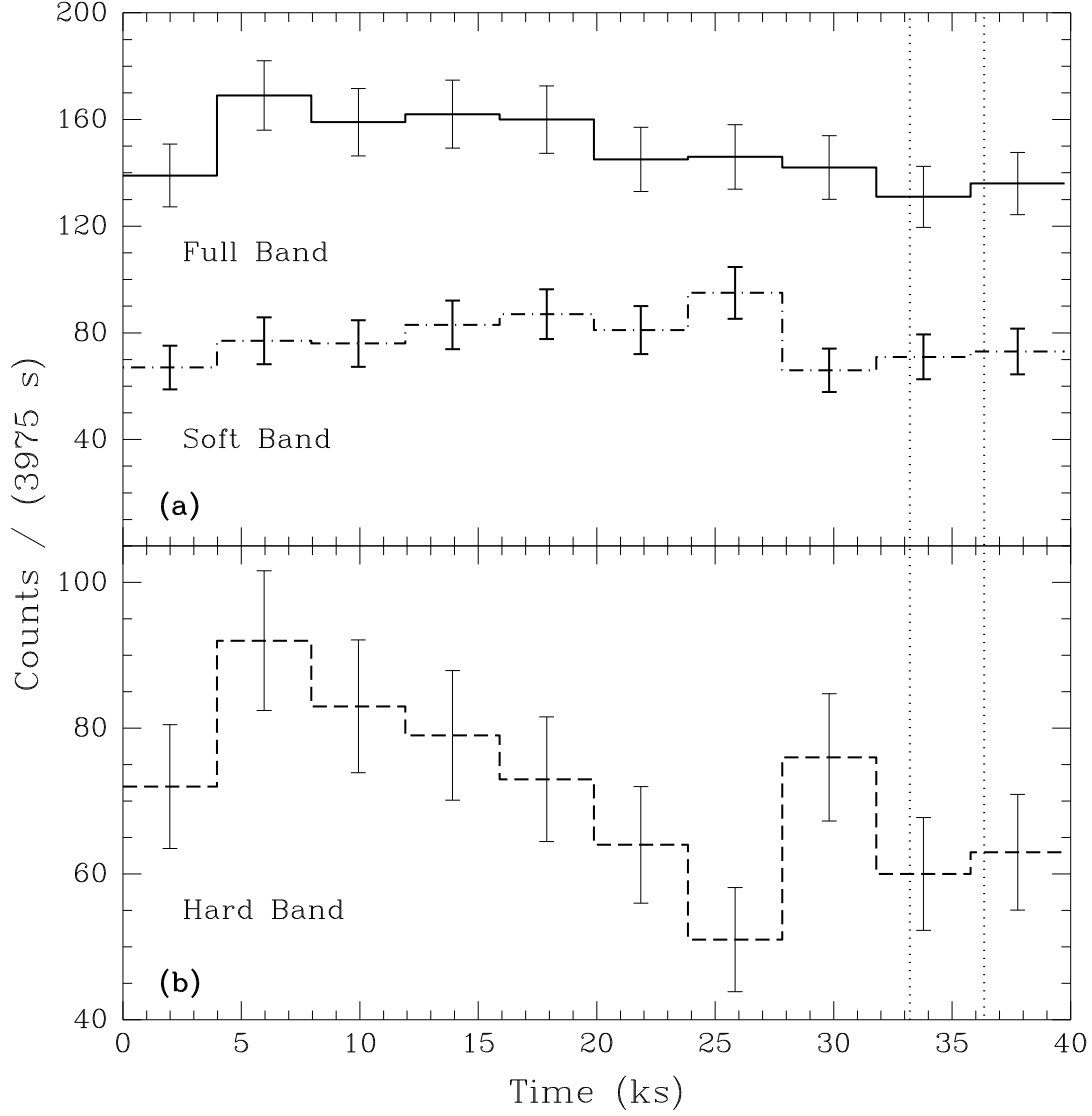
Fig. 7.— Light curves for the nucleus of Mrk 231 extracted from a circular region with a 2″ radius. Each time bin has a width of 3975 s; the background is expected to contribute $\lesssim 1$ count per bin. Error bars are the square root of the number of counts in each bin. The background flare region (see §2) is indicated with vertical dotted lines. **(a)** Full-band and soft-band light curves shown as solid and dot-dashed curves, respectively. While the full-band light curve shows some indication of decreasing flux over the course of the observation, the soft-band light curve is consistent with a constant count rate. **(b)** Hard-band light curve (dashed line) clearly indicating a count rate decrease of $\approx 45\%$. Note that the vertical axis does not extend to zero.
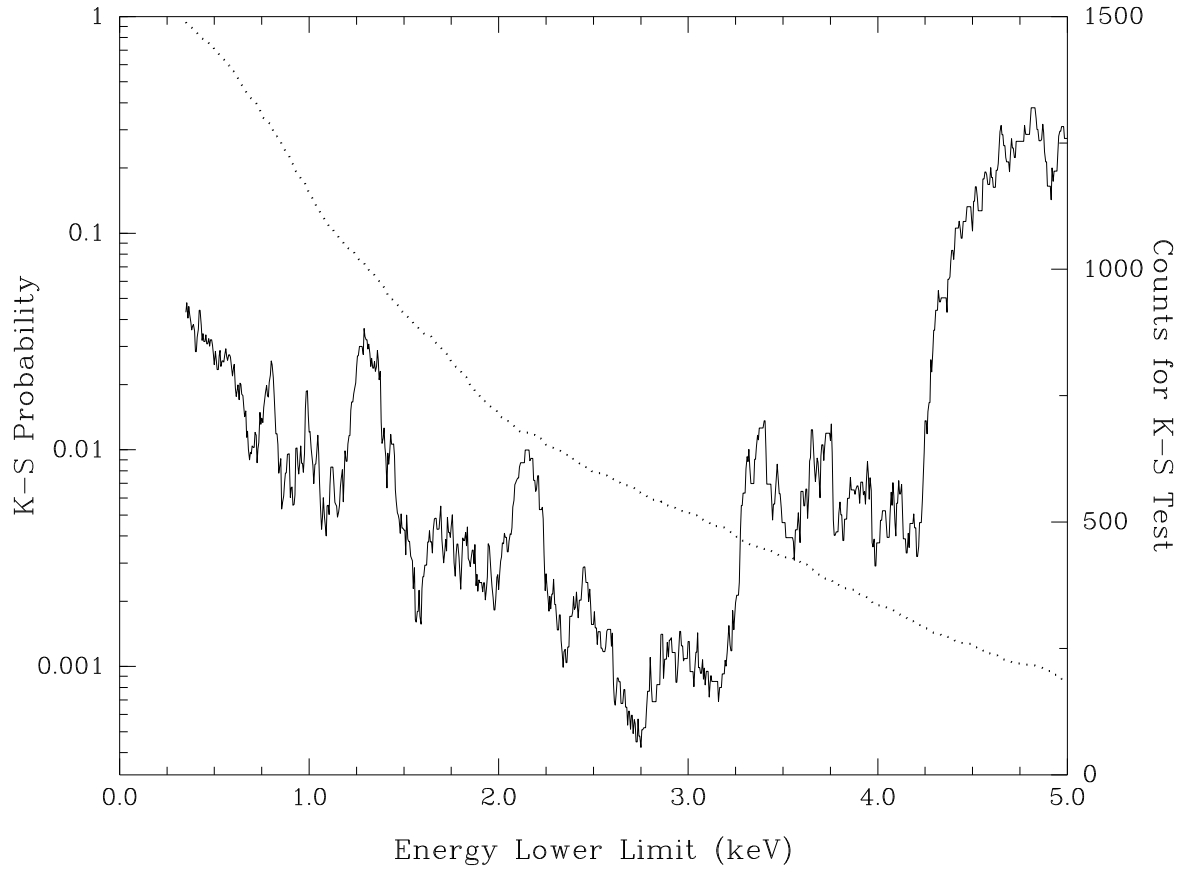
24

Fig. 8.— The solid curve shows the K-S probability as a function of the lower limit on the energy band to which the K-S test was applied; all energy bands extend to an upper bound of 8.0 keV. The most significant variability is indicated by the minimum value of the K-S probability, 4.2×10^{-4}, for an energy band of 2.75–8.0 keV. The dotted curve (associated with the right vertical axis) shows the number of counts used in the K-S test in each energy band. Above an energy lower limit of $E \approx 4.25$ keV, the calculated significance decreases sharply as the number of counts used in the K-S test drops.
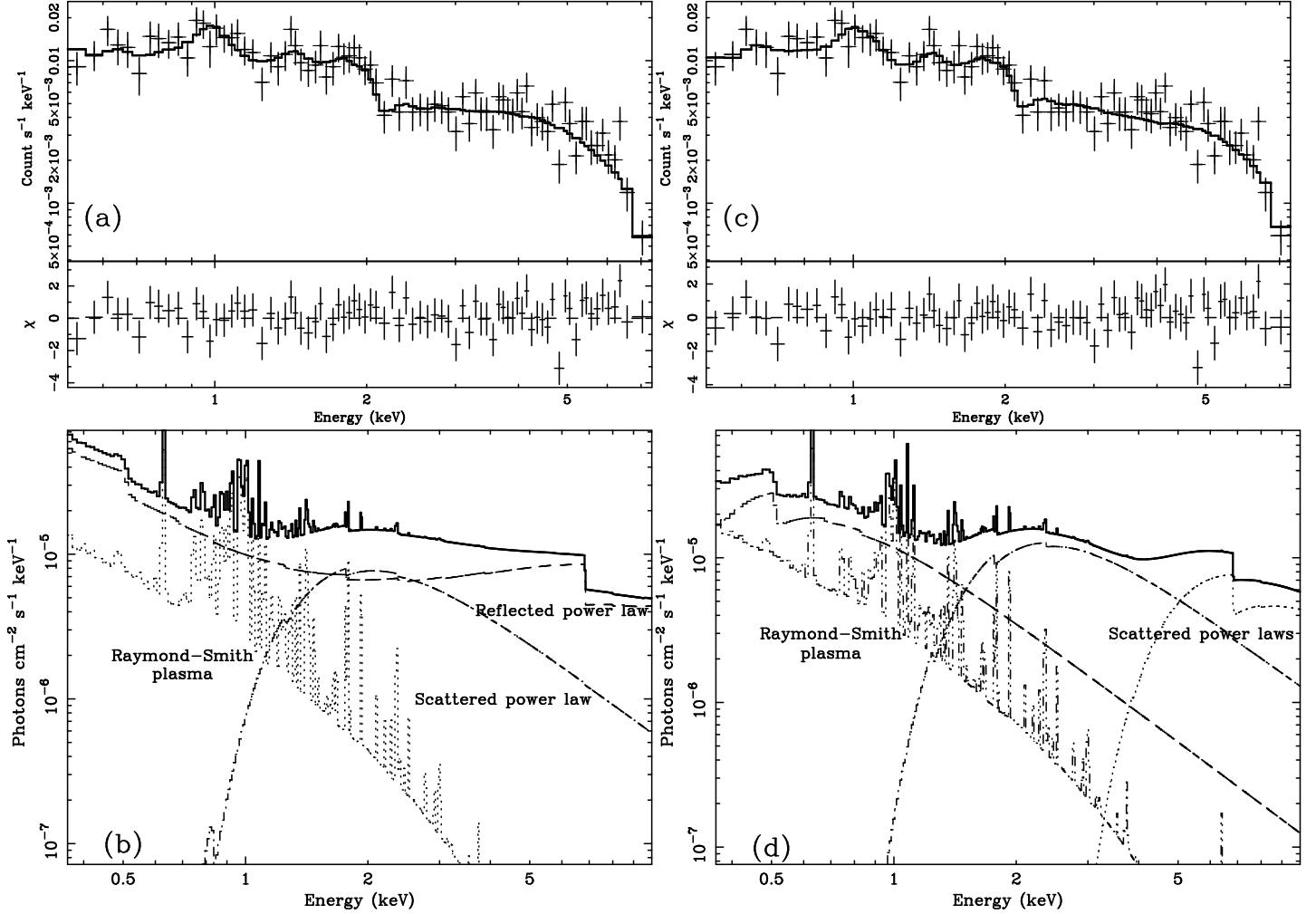
Fig. 9.— **(a)** Observed-frame *Chandra* ACIS-S3 spectrum of the nucleus of Mrk 231 fit with a reflected power law, a scattered and absorbed power law, and a Raymond-Smith plasma (model 4 in Table 2). In both **(a)** and **(c)**, plain crosses are the data points, and the solid curve represents the best-fitting model. The ordinate for the lower panel, labeled χ, shows the fit residuals in terms of σ with error bars of size one. **(b)** Best-fitting reflection-dominated model for the nuclear data. **(c)** Observed-frame *Chandra* ACIS-S3 spectrum of the nucleus of Mrk 231 fit with three absorbed power laws and a Raymond-Smith plasma (model 5 in Table 2). **(d)** Best-fitting model with multiple absorbed and scattered power laws for the nuclear data.
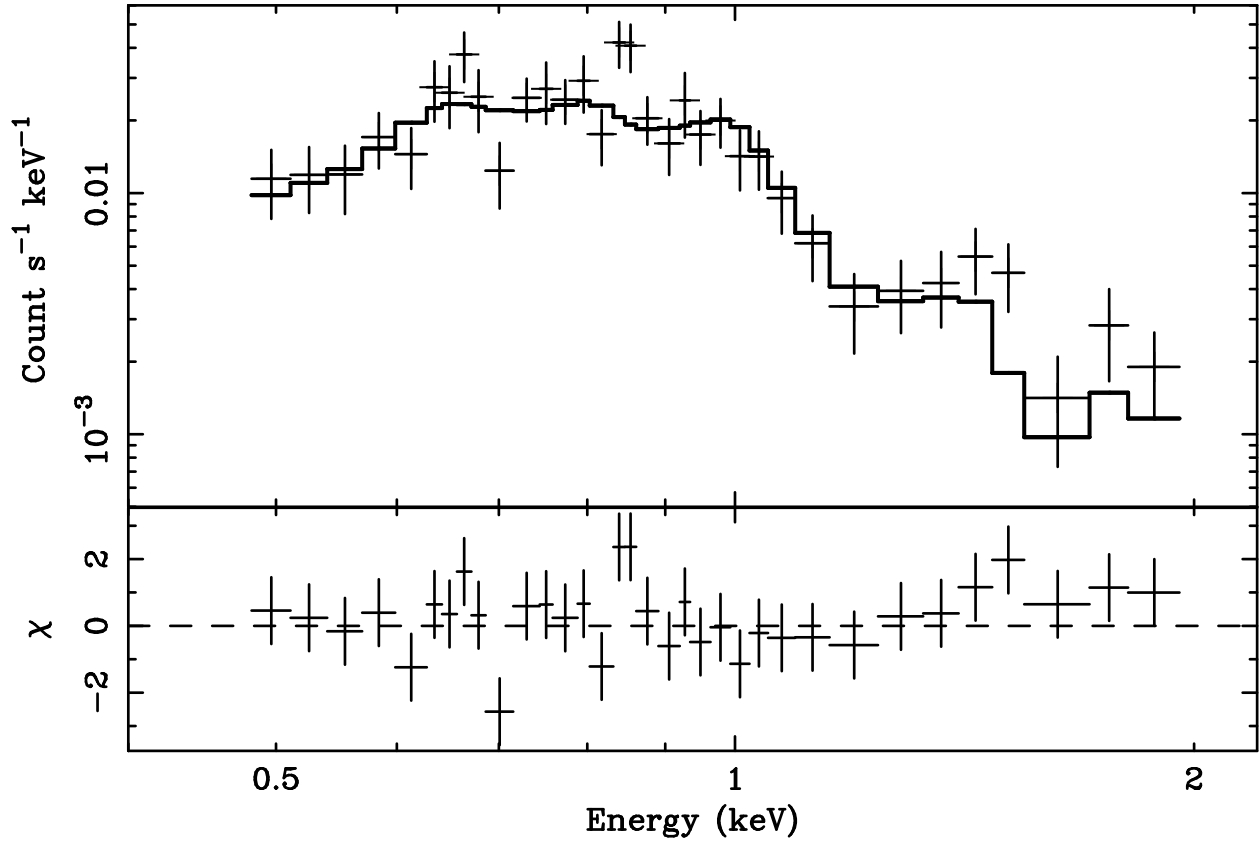
Fig. 10.— Observed-frame *Chandra* ACIS-S spectrum of the extended galaxy emission of Mrk 231 fit with two Raymond-Smith plasmas (see Table 2). Plain crosses are the data points, and the solid curve represents the best-fitting model. The ordinate for the lower panel, labeled χ, shows the fit residuals in terms of σ with error bars of size one.
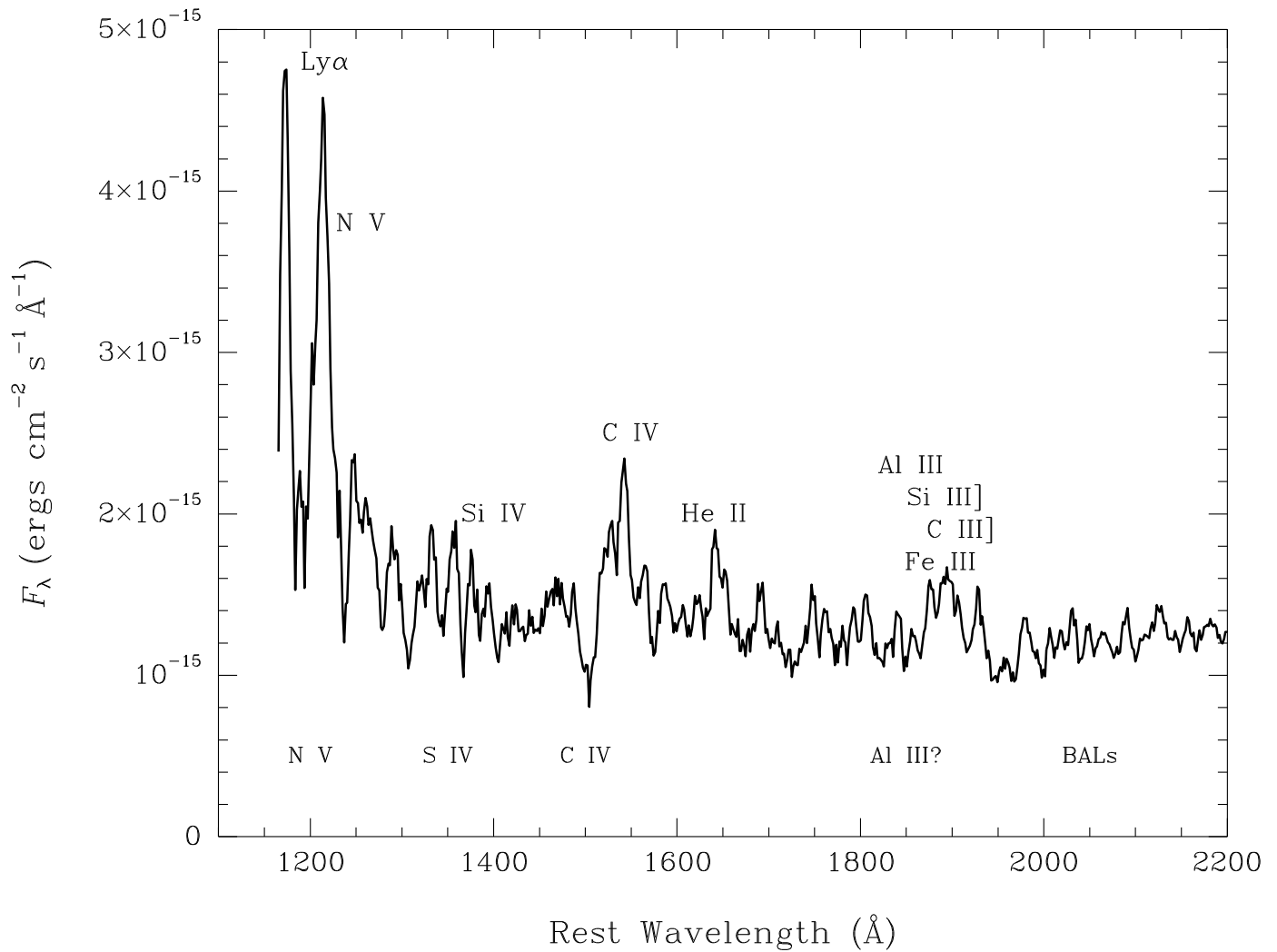
Fig. 11.— Rest-frame *HST* ultraviolet spectrum of Mrk 231. This 770 s FOS calibration observation was taken with the 1″ aperture and the G190L grating. The data have been smoothed with a boxcar filter, and they have not be corrected for Galactic reddening.
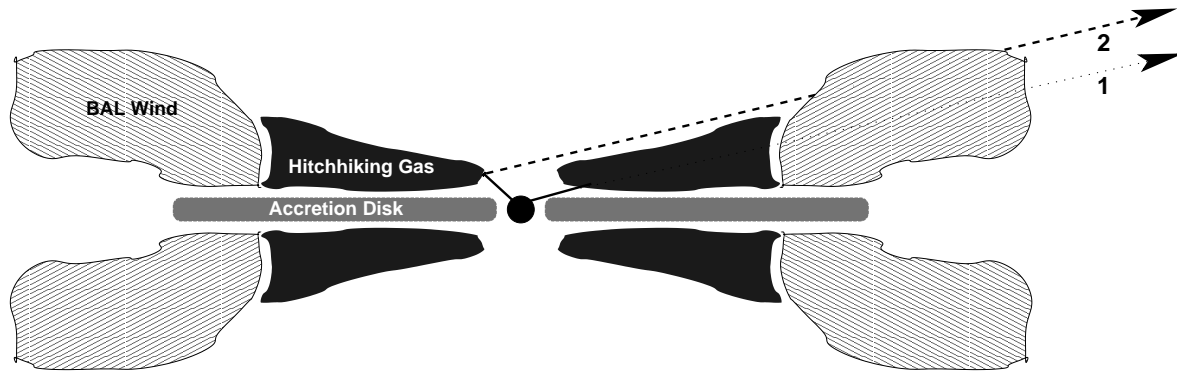
Fig. 12.— Diagram of a possible geometry for the nucleus of Mrk 231 (see §5.1.4 and §6.1.2). The filled black circle represents the black hole and X-ray emitting region. The region marked "Hitchhiking Gas" has $N_H \gtrsim 10^{24}$ cm^{-2}, thus completely blocking direct X-rays at least up to ~ 8 keV. Two lines of sight are labeled: (1) the direct continuum, which is completely blocked, and (2) the scattered continuum exhibiting the observed X-ray variability. This second component is observed to be absorbed with $N_H \sim 10^{22}$ cm^{-2}, perhaps by the BAL wind launched at distances $\gtrsim 10^{16}$ cm. Note that the hitchhiking gas would have to be virtually dust free to enable any optical and ultraviolet continuum to reach the observer. The other two scattered lines of sight implied by the spectral fitting (§5.1.4) are not shown in this figure, but they would have similar paths to (2) (though their scattering regions could be on larger scales).

This figure "f1.jpg" is available in "jpg" format from:

http://arXiv.org/ps/astro-ph/0112257v2

This figure "f2.jpg" is available in "jpg" format from:

http://arXiv.org/ps/astro-ph/0112257v2

This figure "f4.jpg" is available in "jpg" format from:

http://arXiv.org/ps/astro-ph/0112257v2